Master's thesis

NTNU
Norwegian University of Science and Technology
Faculty of Engineering
Department of Marine Technology

Randi Kyllo Ødegård

Fatigue Monitoring of Crane Foundations

Master's thesis in Marine Structures
Supervisor: Sigmund Kyrre Ås
Co-supervisor: Ola Moen
June 2023

NTNU
Norwegian University of
Science and Technology

Randi Kyllo Ødegård

Fatigue Monitoring of Crane Foundations

Master's thesis in Marine Structures
Supervisor: Sigmund Kyrre Ås
Co-supervisor: Ola Moen
June 2023

Norwegian University of Science and Technology
Faculty of Engineering
Department of Marine Technology

NTNU
Norwegian University of
Science and Technology

Preface

The following report presents work conducted for a Master's thesis in Marine Technology at the Norwegian University of Science and Technology (NTNU), specializing in the discipline of Marine Structures. The thesis focuses on an exploratory study that investigates the fatigue damage of welded flanges on crane foundations on aluminium service vessels used for sea farming operations in the Norwegian coastal area.

During the initial stages of formulating the thesis topic, I discussed various topics with Associate Professor Sigmund Kyrre Ås. It was during these discussions that Moen Marin introduced the suggestion of implementing a stress monitoring system on a vessel. Through further dialogue with Ås, we were able to define the specific focus and objectives of this thesis.

I would like to express my deepest gratitude to my supervisor, S.K. Ås, whose insights have been essential throughout this project. His expertise have played an important role in shaping the content and structure of this thesis, enabling me to explore the subject matter in a comprehensive manner. Furthermore, I extend my appreciation to Moen Marin AS for their collaboration on this project. I would like to extend special thanks to Ola Moen for his support in terms of installation and implementation of the monitoring systems. Additionally, I am grateful to Knut-Ola Martinussen from Marin Design AS for generously sharing his knowledge about structure and strength analysis. His expertise has significantly enriched the research and analysis presented in this thesis, providing valuable insights and a broader perspective.

The completion of this Master's thesis would not have been possible without the support and contributions of these individuals and organizations. Their guidance and assistance have greatly enhanced the quality of the research, and I am sincerely thankful for their invaluable contributions.

Abstract

This thesis focuses on evaluating the fatigue damage of welded flanges on crane foundations for service vessels used in sea farming operations along the Norwegian coastal area. The objective of this study is to investigate stress monitoring techniques on this type of vessels and perform a fatigue life assessment.

Stress data is collected using strain gauges installed on the crane foundation. Pressure data from the crane is also measured using a pressure sensor, and the motion and acceleration of the vessel is monitored using an IMU. The data from the pressure sensor is used to verify the validity of the strain gauge measurements. As the strain gauges are installed at different locations on the crane foundation, stresses from the gauges are expected to change due to usage of the crane in different directions.

The measured stress data is used to calculate the fatigue life based on two different sets of recommendations: Eurocode 9 and International Institute of Welding (IIW) recommendations. Hot-spot S-N curves for each recommendation are established, which requires that finite element models are made for the crane foundation and the welding detail. These are made in Autodesk Inventor Professional and Abaqus, respectively.

The results reveal significant differences in fatigue life predictions between Eurocode 9 and IIW recommendations. Eurocode 9, known for its conservative approach, yields shorter fatigue life estimates, while IIW recommendations allow for longer fatigue life predictions. The study discusses the difference in fatigue life predictions between the two standards.

It is concluded that the calculated fatigue life in different aluminium structures are widely different depending on the standard that is used. This emphasize the need for further research and exploration of fatigue analysis methodologies and standardization. This study gives a better understanding of how to monitor stress and assess the fatigue performance of welded flanges on crane foundations. It provides a starting point for future research to improve methods of evaluating fatigue life and enhance the design and safety of marine structures used in sea farming operations.

Sammendrag

Denne avhandlingen fokuserer på evaluering av utmattingsskader på sveisede flenser på kranfundamenter på servicefartøy som brukes i operasjoner i oppdrettsnæringen langs norskekysten. Målet med studien er å undersøke teknikker for spenningsovervåkning på denne typen fartøy og gjennomføre en vurdering av utmattelseslevetiden.

Spenningsdata samles ved hjelp av strekklapper som er installert på kranfundamentet. Trykk fra kranen måles også ved hjelp av en trykksensor, og fartøyets bevegelse og akselerasjon overvåkes med en IMU. Dataene fra trykksensoren brukes til å verifisere gyldigheten av målingene fra strekklappene. Siden strekklappene er installert på ulike steder på kranfundamentet, forventes det at belastningene som måles vil variere avhengig av kranens bruk i forskjellige retninger.

De innsamlede spenningsdataene brukes til å beregne utmattelseslevetiden basert på to forskjellige anbefalinger: Eurokode 9 og anbefalingene fra International Institute of Welding (IIW). Det etableres hot-spot S-N-kurver for hver anbefaling, noe som krever opprettelse av elementmodeller (finite element models) for kranfundamentet og den relevante sveisdetaljen. Disse modellene blir laget i henholdsvis Autodesk Inventor Professional og Abaqus.

Resultatene viser betydelige forskjeller i forutsett utmattelseslevetid mellom Eurokode 9 og IIW-anbefalingene. Eurokode 9, kjent for sin konservative tilnærming, gir kortere estimater på utmattelseslevetiden, mens IIW-anbefalingene forutsier lengre utmattelseslevetid for samme konstruksjon. Studien diskuterer forskjellene i utmattelseslevetidsforutsigelsene mellom de to standardene.

Konklusjonen er at beregnet utmattelseslevetid i ulike aluminiumsstrukturer er betydelig forskjellig avhengig av hvilken standard som brukes. Dette understreker behovet for videre forskning og utforskning av metoder for utmattingssanalyse og standardisering. Studien gir bedre forståelse for hvordan man kan overvåke spenning og vurdere utmattingsytelsen til sveisede flenser på kranfundamenter. Den legger grunnlaget for fremtidig forskning med mål om å forbedre metoder for evaluering av utmattelseslevetid og forbedre design og sikkerhet for marine konstruksjoner som brukes i oppdrettsoperasjoner.

Table of Contents

Introduction

Fish Farming Industry

Fish farming, also known as aquaculture, is an important and rapidly growing industry worldwide. The Asia-Pacific region is by far the largest producer of farmed fish, accounting for around 90% of the global production. China is the world's largest producer of farmed seafood, responsible for around 55% of the global total. Other major producers in the region include India, Indonesia, Vietnam, and Bangladesh. In addition to the Asia-Pacific region, Europe is also a significant producer of farmed seafood, accounting for around 6% of global production. Norway is one of the largest producers in Europe, along with countries such as Greece, Spain, and the United Kingdom [1].

The Norwegian fish farming industry is no more than 45 years old. Over the course of these years, the industry has developed from being a small, supplementary industry at the start, to becoming an industrial and high-tech industry with an annual turnover of more than NOK 80 billion today [2]. Norway is particularly well-suited for fish farming due to its long coastline, numerous fjords, and cold waters. These conditions provide an ideal environment for fish to thrive. The fjords in particular offer sheltered areas where fish can be farmed in a relatively controlled environment, protected from rough seas and strong currents. These areas are also ideal for regulating water quality and controlling the spread of disease, as well as providing easy access for transportation and logistics [3][4].

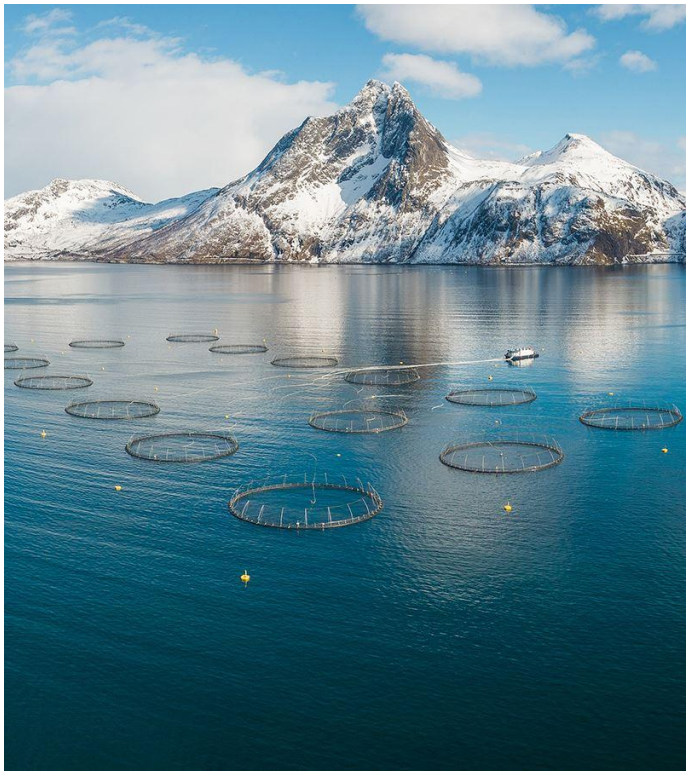

Figure 1: One of Salmar's fish farming facilities.

Service vessels

To operate the aquaculture facilities, service vessels are absolutely necessary. They are used in various operations, such as surveillance, inspections, net cleaning, mooring, ROV operations, diving services and removing of sea lice [5]. To perform all these operations, the service companies are depending on their vessels to be operational. A vessel in the sea is exposed to waves, winds and

different concentrated loads. Not only the highest expected load, known as the ultimate load state (ULS) needs to be accounted for in the design process, the vessels are also susceptible for fatigue loading. Fatigue occurs in structures when they are exposed to cyclic loading and unloading. As the fatigue loading of waves and wind are stochastic by nature, and the concentrated loads are hard to predict, there are several uncertainties that needs to be accounted for, which results in conservatism in the design process. To decrease the structural costs of a vessel, more knowledge is required about the actual damage of the design fatigue life.

The use of equipment on vessels used in operations in aquaculture is not necessarily in accordance with all requirements and recommendations. There are for instance no legislation that requires courses for crane operators on vessels that operates in enclosed waters. The only requirement is that the operator is at least 18 years old and has received adequate training [6]. When performing different tasks on a sea farm, such as mooring operations or net replacements, heavy crane lifts are performed. Experience shows that the cranes are often used for towing, which they are not intended to, as well as they are used in heavier operations than intended. Cranes are usually installed with a mechanical lock that prevents the crane from applying greater torque when the safe working load (SWL) limit is reached. However, it is a known fact that operators use the acceleration and roll motion in waves to apply even greater forces to the crane. The initial force is also increased by the acceleration of the vessel in waves. Repeatedly use of a vessel in heavier operations than it is designed for have resulted in cracks in the weld on the flange on some vessels' crane foundations. It is therefore suggested that further investigation is needed to understand the causes of this fatigue failure.

On the flange on the crane foundation vertical forces tends to concentrate when the crane is used in different operations. Fatigue cracks is more likely to develop in welds, thus it is necessary to assess the fatigue life in these regions. How the crane foundation needs to be designed depends on the concentrated loading due to use of the crane together with the cyclic loading from waves. In the crane foundation, loading from crane operations will contribute most to fatigue failure.

Gaining insights into damage behavior gives the potential to optimize both the design and operational phases of a structure. In the design phase, new information could result in a more cost-effective approach. During the operational phase, opportunities exist for optimizing the utilization of the substructure. However, to gain more knowledge about the fatigue damage, accurate data on the structural stresses are required. In this thesis, the fatigue life of the welded flange on the crane foundation on a small service vessel used in aquaculture is going to be estimated by use of collected fatigue data together with finite element analysis. The test is done in full scale on a service vessel delivered by Moen Marin AS. Finite element analysis is performed to find the ratio between the strain at the measured locations and in the hot-spot, as well as to establish a hot-spot S-N curve which is used to calculate the fatigue life.

Figure 2: The vessel used in this set-up is Fosna Sirius. It is owned by Abyss, designed by Marin Design AS and delivered by Moen Marin AS.

Outline

Several topics will be covered in this report. Chapter 1 focuses on literature on fatigue life of aluminium structures, assessment techniques of in-service stresses and different sensor systems, that together provides background information as basis for the design of an assessment system for the fatigue damage of a vessel. Sections from this chapter are more or less taken directly from the pre-project conducted during the autumn of 2022. Chapter 2 covers the methodology that is applied in the design of the stress measurement system. This includes the set-up for the full scale test together with method for post-processing of the collected data and fatigue calculation. Then in Chapter 3 an overview of the finite element method is given together with the procedure for modelling the finite element models used in this set-up. Further, in Chapter 4 the results of the full-scale test is presented together with the fatigue calculations before these are discussed in Chapter 5. In Chapter 6, a conclusion is finally given and recommendations for implementation and further research are noted.

1 Literature Survey

1.1 Fatigue in Aluminium Structures

The basic topics related to fatigue design of aluminium structures will be covered in this section, together with an overview of necessary input for fatigue calculations and a description of how the design accounts for uncertainties. Fatigue is typically caused by cyclic loads that are less than the yield stress of a given material. It is a cycle by cycle process in which damage accumulates over time with each cycle of loading. Although the damage from each individual cycle may be minimal, the high number of cycles that a structure may experience can lead to significant damage over time.

1.1.1 "Safe-life" and "Fail-safe"

In the field of fatigue design, there are two main design approaches: safe-life and fail-safe. The safe-life approach involves designing components or systems to not fail within a specific, predetermined period of time. The typical service load spectra that the structure is expected to experience are determined and used to conduct laboratory tests on the actual component. These tests help estimate the fatigue life of the component, which is then modified by a factor of safety to determine its safe life [7]. In standards, the safety factor is often large to guarantee a safe operating life, even though it is not the most economical or efficient way to design the structure. At the end of the expected life of a component, it is removed from service, even if it has not experienced any failure and still has considerable residual fatigue life [8]. This approach is typically used when it is not possible to conduct inspections or replace components.

The fail-safe approach to fatigue design involves designing structures such that, even if an individual component fails due to fatigue cracking, the remaining parts will still be able to support the structure and maintain its safety until the crack can be detected and repaired. Components with multiple load paths are often considered fail-safe due to their structural redundancy. When using this approach, regular inspections and crack detection techniques are crucial in order to identify and repair any flaws in the structure. The goal of these inspections is to maintain a satisfactory level of structural reliability [7].

When using the fail-safe approach to fatigue design, an inspection plan for cracks is often put in place to ensure the structural integrity of the design. For example, in a ship hull, fatigue cracks tend to develop in the secondary structure. The hull construction is generally tolerant to this type of cracking, so these cracks are seen more as a maintenance issue than a safety concern. To maintain the integrity of the structure, inspections are performed every five years or so, with any necessary repairs performed as needed [8].

1.1.2 Fatigue crack growth for welded joints

As noted earlier, fatigue is a cycle by cycle process where damage gradually accumulates with each cycle over time. Although the damage caused by each individual cycle may be minimal, the high number of cycles that a structure endures can result in substantial damage. For instance, a ship subjected to wave loading may experience upwards of 10^8 loading cycles. While the damage from each cycle may not be detectable, the cumulative damage from all of these cycles can be significant [8].

The fatigue life of a structure is typically divided into three stages:

- Initiation N_i
- Crack growth/propagation N_g
- Final failure

Where the total fatigue life is:

$$N = N_i + N_g \tag{1}$$

The behavior of a structure under cyclic loading depends on the nature of the material and the type of joint. In the case of a welded joint, the crack growth stage is the primary concern, whereas for a machined component, the initiation stage is typically more critical. During the initiation stage, the repeated application of cyclic loads causes microscopic imperfections in the material to propagate and grow into macroscopic cracks [9]. Once cracks have formed, crack growth becomes the focus of attention. It is during this stage the fatigue life is estimated.

For welded joints, the crack growth is primarily dependent on the average properties of the material, rather than the crystallographic structure of a single grain. This is because the fatigue strength of welded joints is largely determined by defects in the weld, also known as ab initio defects. These defects should be avoided, but in a large welded structure like a ship, there is a non-zero probability that defects will be present [8]. The stages of crack propagation is divided into three regions:

- Threshold region
- Paris' regime
- Finite life region

By plotting the crack propagation rate versus the stress intensity range, ΔK, using a logarithmic scale, the plot in Figure 3 is usually obtained. Below the threshold stress intensity factor range, ΔK_{th}, a long crack will not propagate. When ΔK exceeds ΔK_{th}, the crack starts to propagate with a low, but rapidly increasing, crack growth rate. Eventually the propagation reaches the Paris' regime, which is the linear part of the curve. In this phase, crack propagation $\frac{da}{dN}$ versus ΔK is given by Equation 2. When K_{max} approaches the fracture toughness of the material, K_{IC}, unstable crack propagation occurs and the component will fracture within relatively few cycles [10].

$$\frac{da}{dN} = C\Delta K^m \tag{2}$$

In Equation 2, the exponent m is the slope of the curve and C defines its vertical position. It must once again be emphasized that this equation only provides an adequate description of the behavior of the growth rates in the Paris' regime (the mid-range) [11].

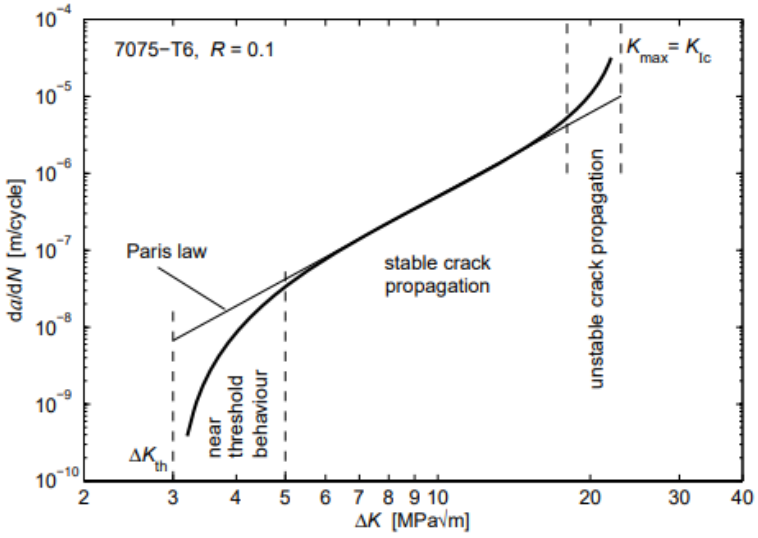

Figure 3: Crack growth rate curve that shows the variation of the fatigue crack propagation rate $\frac{da}{dN}$ with the alternating stress intensity [10].

1.1.3 S-N curve

Tests performed by applying a cyclic stress with constant amplitude on specimens until failure of the specimen have showed a relation between the stress range of a cycle and the number of cycles to failure. The relation is based on a regression curve through numerous results from tests on identical specimens and tends to follow the log-linear relationship formulated in Equation 3

$$N \cdot (\Delta S)^m = Constant \tag{3}$$

where N is the number of cycles to failure, ΔS is the constant amplitude range and m is the Wöhler exponent , which is the slope of the curve. The slope often varies with the number of cycles, as shown in Figure 4. For aluminium structures, m is typically between 3 and 7, depending on material properties, geometry, etc. [12]. The higher the repeated stress level is, the smaller will the number of cycles to failure be [13]. For aluminium, the SN curve will show that the material has a high rate of fatigue, which means that it can withstand many cycles with low stress range before failure. When the stress range increases, the number of cycles to failure will decrease rapidly and the material will be more exposed to fatigue damage.

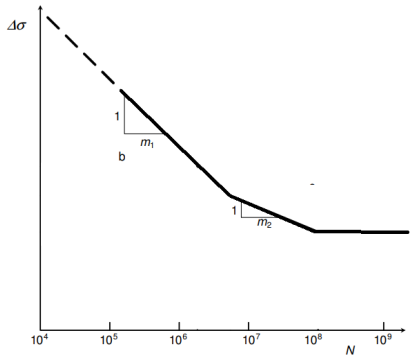

Figure 4: Fatigue strength curve, where $m_2 = m_1 + 2$

The SN curves provides a criterion for determining a safe design stress level for a given target life, under the condition that specific fabrication standards are met. In cases where cracks and defects outside the fabrication standard are found, the SN curve may not provide accurate information regarding the effect on the fatigue life of the structure. Design codes often include multiple SN design curves for various structure details, depending on technological factors, local geometry, load directions and environment. Therefore, the user does not need to attempt to quantify the local stress concentration effect of the weld detail itself. Typically, the design SN curve deviates by two mean standard deviations of log N from published experimental data [14]. In situations where the applied stress on a specimen is low, the fatigue life may be significantly longer than the reasonable testing time. In such cases, a fatigue limit can be defined below which no fatigue damage occurs. However, this concept of a fatigue limit only applies if all the load cycles remain below the limit and in non-corrosive environments [8]. Since ships operate in harsh environmental conditions with high levels of corrosion, the methods used to counteract corrosion must be taken into account when selecting an appropriate SN curve.

1.1.4 Variable amplitude loading

The relationship between constant amplitude stress ranges and the number of cycles to failure is now clear. When conducting field studies in open water or coastal areas, the stress experienced by the structure is variable and the SN-curves from laboratory trials are not directly applicable. It must therefore be determined how the relationship between variable amplitude stress ranges and the number of cycles to failure can be used to find the fatigue damage for a ship.

1.1.4.1 Loading spectra

In order to perform a fatigue analysis of a ship structure, it is necessary to determine a load spectrum that represents the actual loading experienced by the structure. Different loading types contributes to potential failure due to overload or fatigue [15]:

- **Static loads**: The static loads acting on a ship are the loads resulting from differences between the weight and buoyancy distribution along the ship. The weight of items placed inside the ship's hull is not distributed uniformly along the length of the ship. This weight is counteracted by a buoyancy force generated by the water displaced by the ship. The difference between the weight and buoyancy distributions creates shear forces and bending moments along the ship.
- **Low frequency loads**: Low frequency loads acting on ships are mainly wave loads. Wave loads includes both pressure, loads acting on the hull due to the wave profile, and inertial reactions to the accelerations caused by the ship motions.
- **High Frequency Dynamic Loads**: These are loads that may induce vibratory response in the ship structure. Example of high frequency dynamic loads are loads caused by large unbalanced rotating machinery.
- **Operational loads**: Loads generated when the ship performs specific activities, such as crane lifts. These activities can create additional stresses on the ship's structure.

1.1.4.2 Palmgren-Miner

Development of fatigue damage under stochastic loading conditions is termed cumulative damage. In literature, there are many different approaches for computing the cumulative damage caused by fatigue loading. However, the Palmgren-Miner rule is the simplest, and it is proven to be no worse than other methods [11]. This summation rule is based on the hypothesis that the fatigue damage done by one cycle in a constant amplitude stress range, ΔS is given as

$$D = \frac{1}{N} \tag{4}$$

The total fatigue damage is then equal to the accumulated cycle ratio, expressed as

$$D = \sum_i \frac{n_i}{N_i} \tag{5}$$

where D is the damage (where D = 1 in theory corresponds to failure), n_i is the number of applied cycles and N_i is the number of cycles to failure for the i_{th} constant amplitude stress level ΔS [16].

1.1.4.3 Counting

To assess the fatigue damage, it is essential to determine the values for n_i and N_i. To obtain these values, loading amplitudes must be counted. The purpose of cycle counting is to convert a variable amplitude stress sequence into a set of constant amplitude stress range cycles that are equivalent, in terms of damage, to the original sequence. The obtained distribution can be utilised to find the number of cycles to failure for a certain stress range, N_i. Various cycle counting methods have been developed to count the occurrences of different loading amplitudes [17]. However, the quality of the results depends largely on the nature of the input stress history.

Level crossing counting
The method of level crossing counting is illustrated in Figure 5. To halve the number of counted events, positive going level-crossings are recorded at and above the mean value, while negative-going crossings are counted below the mean load. The main limitation of using the level crossing counting method is that it does not provide information about the irregularity of the load. Reversal points are assumed to occur halfway between levels. This means that narrowed-band processes are represented in a realistic way, while broad band loading, where stress ranges have mean values different from the mean level of the loading, are represented in an unrealistic way and the method tends to be conservative. Use of this technique is described in detail by Almar-Næss et al. in Fatigue Handbook [11].

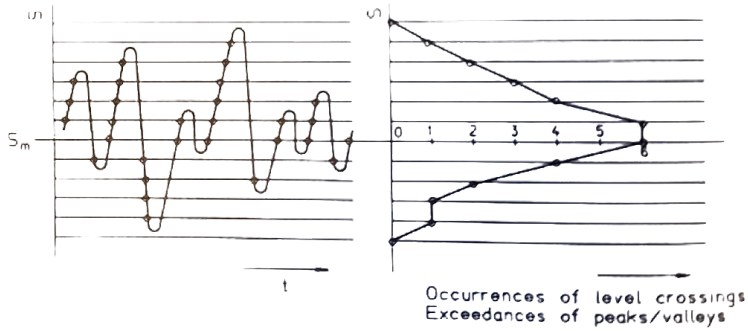

Figure 5: Irregular load-time history converted into occurrence spectra of level crossings. The difference in counts between two adjacent stress levels is equal to the number of peaks or valleys in that interval of stress [11].

Peak counting
When using the peak counting method, the peaks are counted above the mean level while the valleys are counted below. The counted peaks are combined in a plot starting with constructing the largest cycle, then the second largest, and so on. In this way, a conservative count is obtained. An illustration of peak counting is shown in Figure 6.

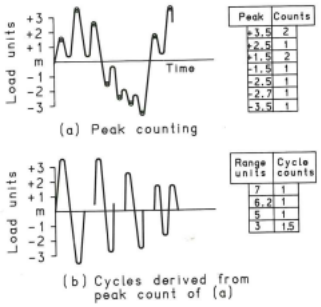

Figure 6: Peak count of a broad banded load history [11]

Rainflow-counting
For ships and offshore structures it is recommended to use rainflow counting, as these structures are exposed to wind and waves that usually results in wide band signals. The method is designed to count reversals in accordance with the material's stress-strain response [11]. Rainflow counting was named from a comparison to rain falling on a pagoda roof and running down the edges of the roof [18]. This technique is explained in more detail in Appendix A.

1.2 Assessment of fatigue

The ideas outlined in Section 1.1 are in combination with expected wave and wind loads used to develop an estimate of the fatigue life for the structure. Fatigue is a complex and unpredictable process, which makes it challenging to model accurately. In this chapter the existing methods for assessing the predicted lifetime of structures are investigated.

1.2.1 Nominal stress method

The nominal stress is the average stress over a given cross-section. It can be determined from classical beam theory or from finite element analysis. The first method may be used for simple structures. The stresses σ_w or τ_w in the weld throat **a** for a given weld length l_w and a force **F** can be calculated using Equation 6.

$$\sigma_w = \frac{F}{A_w} = \frac{F}{a \cdot l_w} \tag{6}$$

The second method is primarily used for complicated hyperstatic structures and for structural components where macro-geometric discontinuities are incorporated. Here, one must ensure that all stress concentration effects from the weld joint itself are excluded when calculating the modified nominal stress [17].

Summarized, the nominal stress approach involves identifying welds that may be critical in a structure and assigning a weld class to them. Which weld class a welded component corresponds to depends on geometry and load configuration. Next, a nominal stress range or spectrum is assigned to each joint. The nominal stress is then multiplied by stress concentration factors and the SN curve corresponding to the weld class is used to determine the fatigue life or damage sum for each joint.

1.2.2 Hot-spot stress method

The fatigue life of a welded structure depends on the peak stresses where the fatigue cracks are expected to develop. The hot-spot is defined as the region where the crack is expected to initiate. In welded tubular joints, these locations are the weld toes, due to large stress concentrations and geometry of the weld. The hot-spot stress is a combination of membrane stresses and bending stresses and includes all stress raising effects, except from the one due to the local weld profile itself. The stress effects from the weld is not included since it is influenced by weld shape irregularities that are highly localized and difficult to quantify and therefore not suitable for systematic stress analysis [11]. At the weld toe, the structural hot-spot stress can be determined by extrapolation of the stress distribution curve from a reference point to the weld toe. The structural stresses are dependent on the global dimensions and loading parameters of the component in the vicinity of the joint [17].

The hot spot stress can be determined by either measurement or calculation. The procedure is as follows:

1. Establish the reference points (two or three depending on the method). The reference points should be located outside the limit where the notch influences the stress distribution. DNV recommends placing the extrapolation points 0.5t and 1.5t ahead of the weld toe [19]. These points are also specified by NORSOK N-004 [20].
2. The hot-spot stress at the weld toe is determined by extrapolation from the stresses in the reference points to the weld toe .

Identification of hot-spots may be done by measuring several different points on a structure, analysing the result of a prior FEM analysis or from experience of existing components, especially if they have failed.

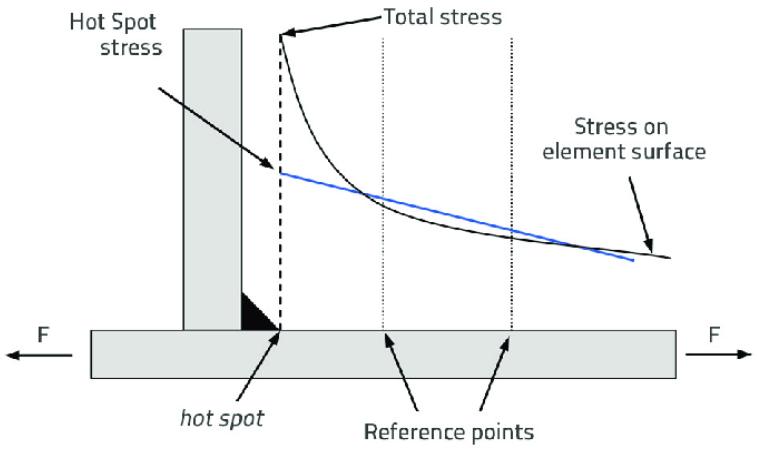

Figure 7: Definition of hot spot stress [21]

1.2.3 Notch stress method

According to DNVGL-RP-C203, the notch stress is the total stress at the root of a notch, taking into account the stress concentration caused by the local notch. Thus, the notch stress consists of a sum of the structural stress and the non-linear stress peak. These are obtained by assuming linear-elastic material behaviour. The actual weld contour needs to be replaced by an effective one in order to take account for variation of weld shape parameters and non-linear material behaviour at the notch root. In order to use this method in finite element analysis, a fine mesh model is required around the notch region [19].

The notch stress method can only be used to assess welded joints with respect to potential fatigue failures from the toe or root of the weld. Additionally, the fatigue assessment must be performed at the weld toes for the parent material using the hot-spot stress and the associated fatigue class (FAT) for the material at the base. The method is not applicable if there is a significant stress component parallel to the weld, nor for other modes of fatigue failure. It should also be noted that the notch stress method is limited to a plate thickness of $t \geq 5$ mm, since it has not been verified for smaller plate thicknesses. At weld toes, an effective notch stress of at least 1.6 times the structural hot-spot stress should be assumed [17].

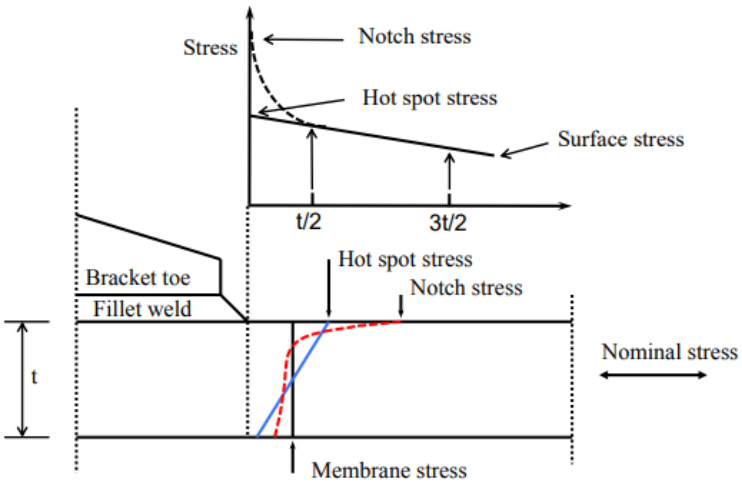

Figure 8: Stress distribution for the nominal stress method, hot-spot method and notch stress method [19].

1.3 Sensors

In Section 1.2 methods to extrapolate or interpolate measured values to unmeasured locations was described. In this chapter it will be focused on what sensors to use in order to do the initial measurements needed for fatigue assessment of a structure.

1.3.1 Strain

Strain sensors may be used to measure static strain due to relatively constant loads or dynamic strain due to transient events or vibration. They allow for a precise determination of the low frequency content of the dynamic response. On the other side, strain sensors will in general have a relatively high noise floor compared to other types of sensors. In this section, two types of strain sensors will be discussed: strain gauges and fibre optic sensors.

Stain Gauges
Electrical strain gauges are devices that are used to measure strain on an object. They are commonly used in a variety of applications, including structural engineering, automotive testing, and aerospace engineering. They typically consists of a wire or a foil that is attached to the surface of the object being measured with a suitable adhesive. They are highly sensitive and can be used to measure very small changes in strain. A typical strain gauge is shown in Figure 9, where the resistance is measured between the terminals.

Short strain gauges are flexible as to where they can be located. Therefore, they are suitable for smaller vessels or vessels with more complex structures and less clear deck area. The location of the gauges are sensitive to localised stress concentration, so care must be taken as to where gauges are placed and how the results are interpreted [15].

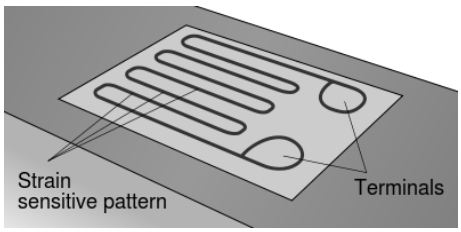

Figure 9: Typical strain gauge [22]

Deformation of the strain gauge results in a change in the resistance through the gauge and can be measured as a change in electrical current or voltage through the sensor. The change is usually measured by a Wheatstone bridge. The Wheatstone bridge can be used in different gradients, but a full bridge is often applied to minimize noise and compensate for temperature changes. The relation between resistance and strain is

$$\frac{V_0}{V_s} = k\epsilon \tag{7}$$

where V_0 is the bridge output voltage, V_s is the bridge excitation voltage, k is the gauge factor and ϵ is the strain [23]. The gauge factor is different for different strain gauges, and is given in the data sheets.

The change in resistance, measured by the Wheatstone bridge, needs to be amplified as it is very small. The voltage difference is typically in the range of microvolts to millivolts, which is too low for most data acquisition devices or display instruments to detect and process. Therefore, an amplifier is needed to boost the signal level. An amplifier is a high performance signal conditioner that can also provide filtering, excitation, calibration and linearization functions [24]. Each sensor must be connected to the unit separately, which can result in a large number of cables for a fully instrumented structure [25].

The mentioned Wheatstone Bridge is a system consisting of a combination of four resistances connected. It can be used to accurately measure unknown resistance values [26]. In Figure 10a R_X is the unknown resistance, while R_1 to R_3 are known. R_x is calculated by using Kirchoff's circuit law and the change in resistance. For strain measurement in one direction, a quarter-bridge can be applied. This is implemented as seen in Figure 10b. One drawback when using this type of Wheatstone bridge is that it does not compensate for temperature, as the full Wheatstone bridge in Figure 10c does [27].

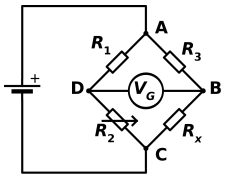

(a) Wheatstone bridge circuit diagram [28].

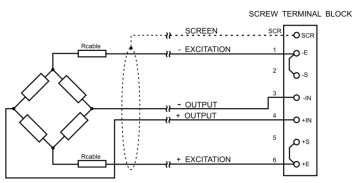

(b) 4-wire Wheatstone bridge [29].

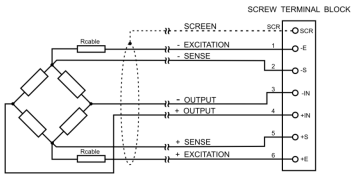

(c) 6-wire Wheatstone bridge [29]

Figure 10: Wheatstone bridges

Fiber optic sensors

A fiber optic strain sensor is a device that uses fiber optical technology to measure the strain on an object. It measures the variation in the light transmission caused by a change in the wavelength due to strain. Its small size, often the diameter of a human hair, makes it practical to use in tight spaces and processes the ability to measure thousands of locations over several meters [30]. When strain is induces, the relative change in Bragg wavelength is:

$$\frac{\Delta\lambda_b}{\lambda_B} = (1 - \rho_e)\epsilon = \Delta V \tag{8}$$

$$\epsilon = \frac{\Delta V}{(1 - \rho_e)} \tag{9}$$

where ϵ is the strain, ρ_e is the effective photo-elastic constant of the fiber core material, λ_b is the Bragg wavelength and $\Delta\lambda_b$ is the change in the Bragg wavelength. Research have proofed that fiber optic sensors shows more accurate results than strain gauges. Other benefits is that the use of light signals eliminates the need for amplification and that the system is passive and relies solely on the light in the fiber, meaning that the sensors do not require electricity and only the interrogator needs power. In "Fibre Bragg gratings in structural health monitoring - Present status and applications", Majunder et al. concluded that although there are several benefits of using fiber optic sensors, they have not reached their full market potential yet, due to high cost of interrogation and lack of standardisation by international governing bodies [31]. Another challenge is encapsulation of the sensors. This needs to be done in an optimal way before industrial application since the optic fibres are too fragile to be installed uncovered. Fiber optic sensors are also strongly temperature dependent, thus temperature compensation needs to be implemented either through temperature measurements or through the use of passive temperature compensation measuring points.

Finally, it can be concluded that optical strain gauges is becoming an attractive and powerful alternative to electrical strain gauges in many fields of applications. This is due to the fact that they are less sensitive to noise of electrical equipment, better suited to withstand harsh environmental conditions and less sensitive to failure caused by fatigue [32].

1.3.2 Gyroscope

A gyroscope senses change in orientation of a device. It determines the angular velocity (ω) and provides information about orientation in pitch, roll and yaw. Gyroscopes are commonly used in a variety of applications, including navigation systems, remote control vehicles, and stabilizing systems. The first gyroscopes was used in the middle of the 19^{th} century and consisted of a simple wheel mounted on 2-3 gimbals. These instruments was limited to its moving parts, and nowadays more modern types of gyroscopes are used.

One type of gyroscope that is often used in conjunction with an accelerometer in an Inertial Measurement Unit (IMU) is the micro-electromechanical-based (MEMS) gyroscope. It operates using a combination of mechanical oscillation and the Coriolis force. The Coriolis force is the inertial force that acts in a direction perpendicular to the rotation axis. One could imagine that there are two capasitive blocks inside the MEMS gyro that oscillates at fixed rates in opposite phases, as shown in Figure 11. When the device is rotated, the blocks' Coriolis force moves them slightly in opposite directions due to the phase difference. The force differences changes the capacitance of the plate underneath it to measure the overall angular rate of an object. The advantages of using the MEMS gyroscope is that it has a smaller form factor than other gyroscopes and it has a significanly lower cost than FOG and RLG. Pao presents a more detailed description of all four types of gyroscopes mentioned in this section [33].

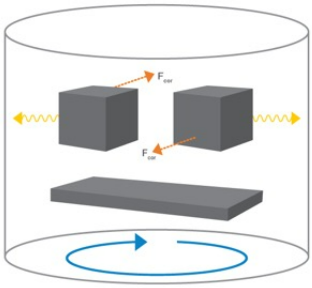

Figure 11: A MEMS gyro consists of two capasative blocks that oscillates at fixed rates in opposite phases.

1.3.3 Accelerometer

To measure the dynamic responses of a large structure, accelerometers are widely used. These devices are good at measuring the high frequency content of the response. Accelerometers has a simple working mechanism as they compare the acceleration they experience with the known acceleration due to gravity. There are several different types of accelerometers and a selection needs to be done based on the expected response and the requirements set for the data. The most common accelerometers are MEMS and piezo [34]. The MEMS accelerometer is essentially a mass suspended by a spring. The direction that the mass is allowed to move in is called the "sensitivity axis". When a MEMS accelerometer is accelerated, the mass will shift to one side, with an equal deflection proportional to the acceleration. When the accelerometer is turned vertically, as shown in Figure 12, both the linear acceleration due to motion and the pseudo-acceleration caused by gravity is measured [35].

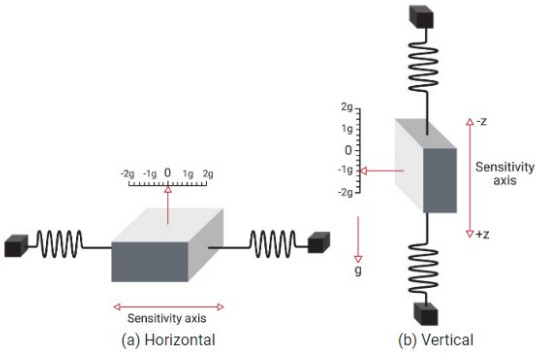

Figure 12: Accelerometer Model [35]

1.3.4 Signal Acquisition and Processing

An important process in a measurement system is data acquisition, which involves sampling signals that measures real-world phenomena and converting them into digital data that can be processed and analyzed by a computer. This data is then used to provide accurate and detailed information about the system being measured. Data acquisition is an important aspect of many measurement systems, as it allows for precise and reliable measurements to be made and sampling frequency, calibration, amplification and recording are topics that are highly relevant.

1.3.4.1 Sampling Frequency

The Nyquist sampling theorem is a fundamental principle of signal processing that states that an analog continuous time signal can be perfectly reconstructed as a digital signal from its samples if the sampling rate is greater than twice the highest frequency component of the signal. In other words, the highest frequency component of the signal needs to be smaller than $f_s/2$, where f_s is the sampling frequency. By fulfilling the Nyquist criterion, it is made sure that the spectrum of the sampled signal is the same as the original spectrum.

To make sure that no frequency in the measured signal is above half of the sampling frequency, the signal can be run through an analog antialias filter before the A/D converter. The ratio between the cut-off frequency, f_c, and the Nyquist frequency, $f_s/2$, is called the oversampling ratio and must be greater than two. A standard oversampling ratio in the field of vibration analysis is 2.56, which ensures that there is room for slope of the filter [36].

The accuracy of strain gauge measurements is easily influenced by many factors. The sampling frequency setting of the measuring device is one of them. If the sampling rate is too low there is a risk of loosing some critical strain values, while a too high sampling rate will increase both the time and cost of data analysis [37].

1.3.4.2 Calibration

Strain gauge signals needs to be calibrated after installation as they are affected by various factors such as temperature, humidity, material properties and installation errors. Calibration is the process of adjusting the output of the strain gauge to match a known standard or reference. The calibration is typically done by using the calibration signal from the measuring amplifier. Amplifiers for strain gauge measurements usually contains a button or a switch that allows a defined signal to be fed into the measurement circuit. There are different methods of calibrating strain gauges, such as shunt calibration and loading calibration. Shunt calibration is carried out by placing a large value resistor in parallel with one of the arms of the strain gauge's Wheatstone bridge to simulate a reduction in the resistance of that arm and a resulting unbalancing of the bridge. Loading calibration is carried out by applying a known force or stress to the strain gauge and measuring its output. Calibration ensures that the strain gauge signals are accurate and reliable for measuring stress levels and distributions in various applications [38][39].

According to Hoffmann, large strains will cause the strain gauges and the Wheatstone bridge circuit to exhibit non-linearities. The non-linearity problem for the Wheatstone bridge are covered in literature, however there is no information regarding the linearity characteristics of strain gauges in the high strain region. These point are further investigated in "An Introduction to Stress Analysis and Transducer Design using Strain Gauges" by Hoffmann. When calibrating the strain gauges using only two calibration points, a linear behavior is assumed. It is also worth noting that long connection cables between the strain gauges and the bridge amplifier will reduce the sensitivity of the measurements. The calibration process using the amplifier's calibration signal does not account for this, but it is sufficiently accurate for short cables [25].

2 Experimental Setup and Procedure

Failure due to fatigue is a highly relevant form of failure that needs to be accounted for in all structures. For ships, it is important to design the different structural components to withstand the effects of cyclic loading, as these structures are exposed to large loads from both wind an waves, together with concentrated loads from execution of different operations. In this chapter, a description of the preparation and execution of full-scale testing to estimate the fatigue life of the welded flange on the crane foundation on a small service vessel used in the sea farming industry is given. This includes test set-up and a description for how to post-process the collected data.

2.1 Experimental set-up

This experiment consists of measuring and evaluation of strain on the crane foundation on a service catamaran used in the fish farming industry, specially focusing on the strain just below the weld on the flange. The setup consists of 10 strain gauges, one Inertial Measurement Unit (IMU), which contains both a gyroscope and an accelerometer, and one pressure transducer that measures the flow through the main cylinder in the crane. The test is to be run for at least a month to capture the use of the vessel in different operations and weather conditions.

2.1.1 Test object

The test is done in full scale on a conventional (diesel engine driven) catamaran in aluminium, operating outside the Norwegian coastal line. The hull dimensioning is according to NBSY 90 [40]. The hull is built with a combined frame system consisting of transverse web frames, longitudinal stringers, three transverse watertight bulkheads and one longitudinal watertight bulkhead to separate the engine rooms. The main dimensions of the vessel, together with the material properties and the plate thicknesses is given below:

Main dimensions	
LOA:	14.99 m
Mld. breath:	12.00 m
Mld. depth to main deck:	3.80 m
Breath pontoons:	4.00 m
Frame distance:	500 mm
Material Qualities	
Plates:	Grade 5083 - H116
Profiles:	Grade 6082 - T6/ Grade 6060 - T6/ Grade 6063 - T5 (Yield strength $>$ 170MPa)
Plate Thickness	
Superstructure/Wheelhouse:	5.0 mm
SB side:	7.0 mm
PS side:	6.0 mm
Deck:	7.0 mm
Hull otherwise:	6.0 mm

As the vessel is used in various fish farming operations, it is equipped with multiple hydraulic deck equipment, which are powered by both the HPU and the PTOs installed on each gear:

Deck crane Palfinger PK90002M H	10T Twister	40+20T Winch
Deck crane Palfinger PK41002(M) G	15T Rope lock	Towing pins
Tenfjord 8-tons capstan	20T Plate lock	Shark Jaw
2 x Tenfjord 3-tons capstan		

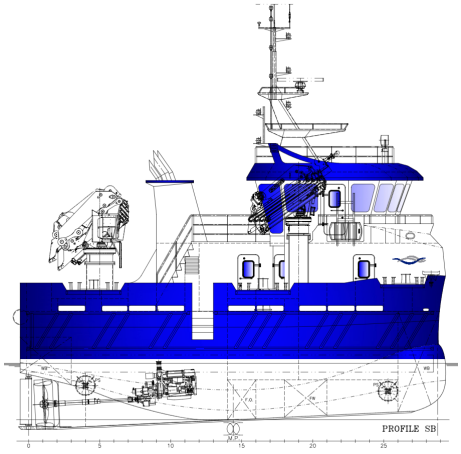

Figure 13: Test object: NabCat1512

The stress measurements covered by this thesis is related to use of the crane of type Palfinger PK90002M, which have a maximum lifting moment of 75.6tm and a continuous rotation in a 360 degree radius. The crane is bolted to its crane foundation which is located on the aft deck as shown on Figure 13. The crane foundation is built in Aluminium 5083-H116 which has a Young's modulus of 71 000 MPa and a Poissons Ratio of 0.33. The structural design details of the crane foundation is given in Appendix B.

2.1.2 Strain gauges

Ten linear strain gauges are installed on the crane foundation, both below deck and under the flange inside the cylinder, as illustrated in Figure 14. The gauges are attached to the vessel with a suitable adhesive. The two strain gauges in Figure 14b is located close to the areas where the highest stresses are found. These high-stress zones are located near the flange outside of the port side of the cylinder; however, as the chosen strain gauges with the used adhesive needs to be installed in a dry environment, they are installed on the inside. The eight gauges below deck are installed to observe how the stress distributes from the cylinder out to the vessel. The strain is measured in both horizontal and longitudinal direction at all locations. The strain gauges used in the set-up was delivered by HBM and has a gauge factor of 2.08.

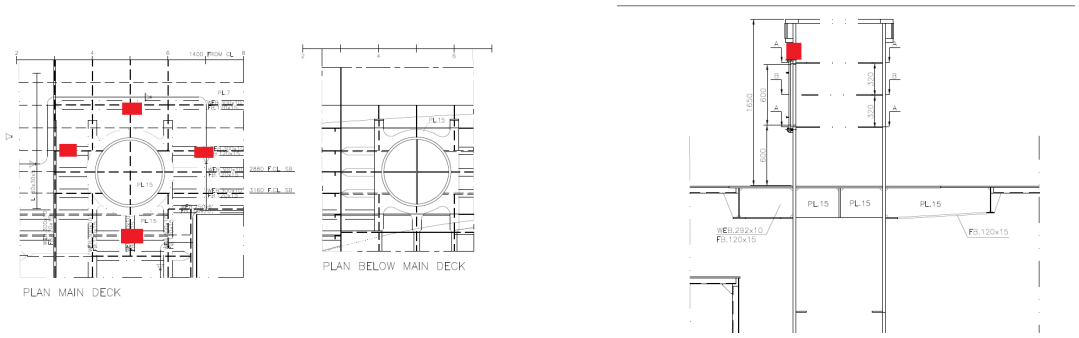

(a) Crane foundation below deck

(b) Inside the crane cylinder

Figure 14: Location of strain gauges

The assumed position of the strain gauges are given in Appendix C. The exact position is not known as the gauges were installed and protected in one operation by a technician that was not instructed to do the measurements, nor given any exact position for the installation. Images of the installed points is shown in Appendix D.

2.1.3 Bridge circuit and amplifier

The strain gauges are inserted as a resistor in a quarter Wheatstone Bridge, as shown in Figure 15a. The quarter Wheatstone bridge is chosen as the force can be applied to the crane in several directions and no angular sensor is installed on the crane. By using a half or a full Wheatstone bridge, the strain measured by the strain gauges would give accurate load pictures only when the strain gauge is fully aligned with the principal strain. The drawback on using the quarter bridge is that it is not temperature compensated and more noise is typically introduced.
The bridge circuits consists of three high precision, high stability resistors from Vishay and one strain gauge. The Vishay resistors was chosen as they have a very low noise and voltage coefficient and an extremely low temperature coefficient of resistance. The quarter Wheatstone bridges are connected to LCD20 amplifiers shown in Figure 15b. This is a compact microprocessor-based unit specially designed to control and monitor weighting applications. It is flexible and allows for connection to most load cells and pressure or strain gauges over a wide range of sensitivities. The amplifier is connected to a power source of 24V and have a bridge exitation voltage of 5V. The output from the amplifier is fully isolated standard analogue outputs of 4-20mA and 0-10V. In this set-up, the 0-10V output is used. To assign desired settings to the LCD20 amplifier the computer program LC Toolkit is used. Table 1 shows the settings used in this test. For the other parameters in the program, the default settings are used.

Category	Setting	Value
Filter	A/D Measurement Rate (samples per second):	80
Calibration	Input sensitivity:	0.5 to 3.7 mV/V
	Decimal point:	19.999
Analogue Output	Output Select:	0-10V

Table 1: Settings in LC toolkit. Settings that are not given in this table are left with their default values.

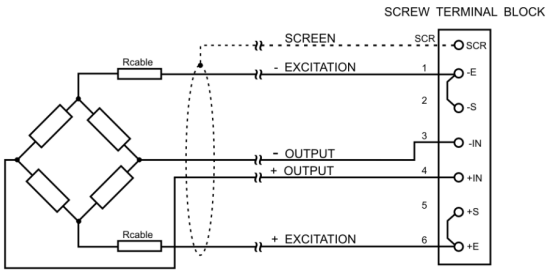

(a) 4-wire Wheatstone bridge with one strain gauge and three fixed resistors.

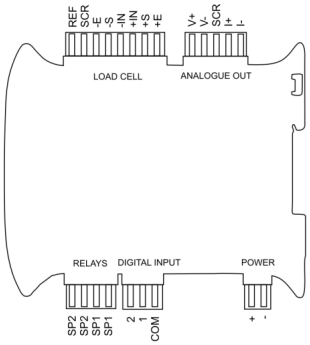

(b) LCD20 amplifier

Figure 15: Wheatstone bridge and amplifier.

2.1.4 Pressure transducer

An Efector500 PT5400 pressure sensor delivered by ifm is mounted in the block on the main cylinder of the crane. The sensor measures in the range of 0 to 400 bars with an analogue output in the range 4-20mA. By using the measured pressure, P, and the internal cylinder diameter, R, the available force in the main cylinder can be calculated by Equation 10.

$$N = \pi \cdot R^2 \cdot P \tag{10}$$

The torque can be calculated by multiplying the force in the main cylinder with the distance from the center of the cylinder to the center of the crane's slewing ring, which is the rotating part of the crane.

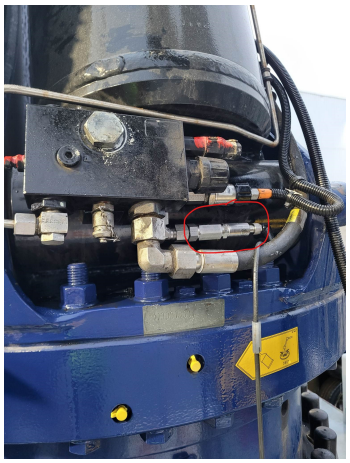

Figure 16: The pressure transducer is coupled to an entrance on the block on the main cylinder of the crane.

2.1.5 Inertial Measurement Unit

An Inertial Measurement Unit (IMU) of type Xsens MTI-630 is mounted at the closest accessible point to the center of gravity (COG) for the vessel with no additional loading and with no trim (Figure 17). The IMU is leveled, which means that it does not show any resulting movement or acceleration when the vessel is floating in still water.

The IMU measures sway, roll and yaw, together with acceleration. This information may be used to monitor the wave conditions that the vessel is operating in, as well as detecting sudden movements or accelerations due to use of e.g. deck equipment or vibrations in the vessel due to machinery.

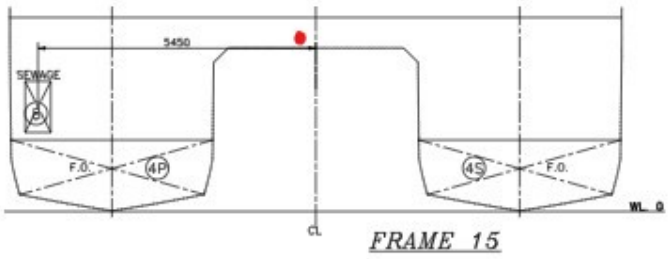

Figure 17: Center of gravity is located at Frame 15, close to the middle of the tunnel. The IMU is installed on the 15^{th} frame.

2.1.6 Data collection

All ten amplifiers are installed in a cabinet located on the wall behind the crane cylinder. One Revolution Pi with three AiO modules are installed in the same cabinet. A Revolution Pi is a type of soft-PLC that works under Linux and can be programmed with different software tools. It is based on Raspberry Pi and can be expanded by various I/O and gateway modules. It is designed to perform real-time control and automation functions in industrial environments [41]. The Revolution Pi collects data provided from the amplifiers, the pressure sensor and the IMU in a frequency of 25Hz and sends it to a Network-Attached Storage (NAS) where the data is stored. Since the NAS is connected to an internet router, the data can be retrieved from outside the vessel.

2.2 Calibration and uncertainties

2.2.1 Calibration

As described in Section 1.3.1, the signal from the strain gauges needs to be amplified as it is too small for the data acquisition device. The LCD20 amplifier is connected to a computer and LC Toolkit is used to amplify the voltage input from the Wheatstone bridge to a value between 0 and 10V. First, loading calibration was attempted. Two calibration points were determined, where the first point was made when no weights were applied and the second was made by applying known weights on the crane. The known weight was the moment in the crane, pointing in starboard direction, when it was locked due to maximum moment. The point with no weights was set to return a value of 5V and the second point was set to return 7.5V. In this way, one could measure both tensile and compressive forces that was larger than the maximum applied calibration load. Due to small deformations and larger variety in temperature, this method gave inconsistent outputs. The amplifier was frequently saturated for most strain gauges, even when the crane was not used. Therefore, another calibration method was attempted, where specified mV/V input values were used for known analogue outputs from 0-10V. The mV/V input values for each strain gauge with the corresponding output value is shown in Table 2.

Strain Gauge	**Input Value [mV/V]**	**Output Value [V]**
SL1	0	0
	2	10
SL2	-1	0
	1	10
SL3	0	0
	2	10
SL4	0	0
	2	10
SL5	0	0
	2	10
SL6	0	0
	2	10
SL7	0	0
	2	10
SL8	0	0
	2	10
SL9	-1	0
	1	10
SL10	0	0
	2	10

Table 2: Specified mV/V input values used for known output values from 0-10V. The corresponding values was determined by evaluating the possible mV/V input from each strain gauge and making sure that these values was located in the chosen interval.

2.2.2 Uncertainties

Several factors can cause uncertainties during strain gauge installation, calibration and amplification using a quarter Wheatstone bridge in the measurement of strain on ships:

Installation and alignment: *Misalignment:* If the strain gauge is not aligned with the direction of the principle strain it will measure a lower value than the actual strain. For example, if the strain gauge is oriented at an angle θ to the principle strain ϵ, it will measure a strain of $\epsilon cos^2\theta$.

Poor adhesion: If the strain gauge is not properly bonded to the surface of the material, it will not transfer the strain accurately and may introduce noise or drift in the measurement. Poor adhesion can be caused by improper surface preparation, incorrect adhesive selection or application, or insufficient curing time.

Damage: If the strain gauge is damaged during installation or operation it will affect its resistance and output voltage. Damage can be caused by mechanical stress, abrasion, corrosion, moisture, dust or electrical overload.

Lead wire effects: If the lead wires are not properly connected to the strain gauge and the amplifier they can introduce errors due to resistance changes, thermal effects or electromagnetic interference [42]. Use of long connection cables between the strain gauges and the measuring amplifier can also reduce the sensitivity of the measurements, leading to increased uncertainty.

Temperature effects: Changes in temperature can cause thermal expansion or contraction of the material, which can affect the strain gauge resistance and output voltage. Temperature can also affect the gauge factor, the bridge balance and the zero offset of the amplifier [43].

Non-linearity and repeatability: The strain gauge and the adhesive layer can exhibit non-linear elastic behavior and time-dependent deformation, which can result in errors when reversing the direction of loading or unloading [44]. These errors are known as hysteresis or reversal error. The strain gauge amplifier may not have a perfectly linear response over the entire range of input voltages, which can cause deviations from the expected output. The amplifier may also have variations in its output for repeated measurements under the same conditions, which can affect the precision of the measurement [45].

Sampling frequency: Sampling frequency can lead to uncertainty if it is too low or too high compared to the bandwidth of the signal. Bandwidth is the range of frequencies that the signal contains. If the sampling frequency is too low, some information may be lost or distorted. This is called aliasing. If the sampling frequency is too high, some noise may be introduced or amplified [46].

To reduce these uncertainties, several measures can be made:

Installation and alignment: *Alignment:* Using a template or a marking tool to align the strain gauge with the direction of the principle strain. Alternatively, using a rosette strain gauge that can measure strain in multiple directions.

Adhesion: Following the recommended steps for surface preparation, adhesive selection and application. Using a suitable adhesive for the material and temperature range. Applying a uniform thin layer of adhesive to avoid air bubbles or excess glue.

Protection: Using a protective coating or a sealed housing to isolate the strain gauge from environmental factors that can cause damage. Avoiding excessive loading or bending of the material that can overstress the strain gauge.

Lead wire connection: Using soldering or crimping to connect the lead wires to the strain gauge terminals. Using shielded wires to reduce electromagnetic interference [42].Use short connection cables to minimize loss of sensitivity.

Temperature effects: Using a temperature sensor or a dummy strain gauge to measure and correct for the temperature effects on the strain gauge resistance and output voltage [43].

Calibration: Using a reference standard or a known input to adjust and verify the accuracy and linearity of the strain gauge amplifier over the desired range of measurement [45].

Methodology: Using a systematic approach to estimate and minimize the strain gauge measurement biases and uncertainties based on experimental data and finite element analysis [47].

Sampling frequency: To minimize uncertainty, the sampling frequency should be at least twice the bandwidth of the signal. This is called the Nyquist criterion [46].

In the set-up covered by this report, several of these factors are relevant. The installation and alignment was performed by a technician from Urdal Services. It is difficult to determine if any faults where done. Any uncertainties due to installation and alignment are also difficult to quantify. As a quarter Wheatstone bridge is used, the temperature effects can be large. It was decided not to use a temperature sensor as the temperature in starboard engine room is quiet constant during operation of the vessel. However, a temperature sensor could have been installed inside the crane cylinder, as the temperature here is more dependent of the outside temperature. A dummy gauge was not used since the crane can rotate and the direction of the principle strain changes with the direction.

As described, the strain gauges are calibrated to log input values in a certain interval. If the input is outside the given area, information will get lost. Calibration of the strain gauge does not include any filtering. The cables from strain gauges SL3-SL10 are shorter than 3m, while the cables for SL1 and SL2 is approximately 4m. This can reduce the sensitivity of the measurement. Another concern is the sampling frequency. A sampling frequency of 80Hz is used for the amplifier and 25Hz for the Revolution Pi. The common range of wave frequencies is between 0.03 and 1.5 Hz, which corresponds to wave periods about 0.2 to 9 seconds [48]. The Nyquist criterion is therefore fulfilled with regards to wave motions. The concern is that the sampling frequency is too low to log impulsive loads in the crane accurately. When the crane is being used in heavy lifts, fast on/off loading or sudden drops may be lost in the sampling process.

2.3 Post Processing and Computational Modeling

Post-processing of the measured data is necessary to calculate stress cycles needed in the fatigue assessment. As the area of the structure that experiences the most stress is typically the weld toe, the hot spot stress is used in the calculations of the fatigue life. To apply the hot-spot method accurately, it is necessary to establish a hot-spot S-N curve for the specific weld geometry and structure used in the experiment.

2.3.1 Post processing

Strain gauges are used to measure small changes in voltage [V] between the terminals of the gauge, and the data is stored in a data acquisition system (NAS). However, to calculate the fatigue life, the required signal is a change in stress [MPa]. Additionally, the installed pressure transducer records the current [A] during the experiment, which must be converted to pressure [bar] to determine the force and torque exerted on the crane. Processing of the collected data is therefore necessary and several steps is needed to transform the raw data collected from the strain gauges and pressure transducer into the relevant parameters required to calculate the fatigue life of the structure.

Stress measurement:
For the strain gauges, the following procedure is followed:

- As the signal from the strain gauges are amplified, it must be divided by the gain to obtain the actual change in voltage. In this case it means dividing the signal by 5.
- The strain can be calculated from Equation 11

$$\epsilon = 4\frac{\frac{V_0}{V_e}}{k} \tag{11}$$

  where V_0 is the measured change in voltage, V_e is the excitation voltage (5V) and k is the gauge factor (=2.08). The expression is multiplied by four as quarter Wheatstone bridges are used.

- The stress can then be calculated:

$$\sigma = E\epsilon \tag{12}$$

  where E is the Young's modulus, which is 71000MPa for Aluminium 5083-H116, and ϵ is the strain.

- Rainflow counting with a threshold value should then be performed. By setting a threshold value, cycles below that threshold are disregarded during the rainflow counting process. This is done because small stress cycles may have negligible effects on the fatigue life of the component. Including these small cycles in the counting process can potentially overestimate the fatigue damage.

Pressure sensor:
As the pressure sensor that is used provides an analogue output between 4-20mA and has a measuring range from 0-400 bar, the relation between current and pressure is assumed linear and the conversion is

$$P = I \cdot 25 - 100 \tag{13}$$

where I is the current. Equation 10 should then be used to calculate the available force in the cylinder. This can be multiplied by the distance from the rotational center of the crane to the center of the cylinder to obtain the torque.

2.3.2 Computational Modeling

More accurate estimations of the fatigue life of the assessed weld toe on the structure under cyclic loading conditions is done when using the hot-spot S-N curve for the structure. It can be established in different ways:

1. By subjecting a sample of the material with the specific weld geometry used in the experiment to cyclic loading while monitoring the number of cycles it can endure before failure. The information can be plotted to a graph to create the S-N curve.
2. By using the Hot-spot reference detail method proposed in Eurocode 9 and Recommendations for Fatigue Design of Welded Joints and Components from IIW [49][17].

As the first option requires both test specimens and laboratory facilities, the second one was chosen to establish the hot-spot S-N curve. The difference between the methods in Eurocode 9 and in the IIW recommandations is the FAT-value for a welded joint and the slope of the S-N curve. Eurocode 9 is a European standard that provides guidelines for the design of aluminum structures susceptible to fatigue. On the other hand, IIW Recommendations for Fatigue Design of Welded Joints and Components is a set of guidelines published by the International Institute of Welding (IIW) on fatigue of welded components and structures. The IIW recommendations are based on extensive research and testing, while Eurocode 9 is based on a more conservative approach [50].

The hot-spot reference detail method is described in both Eurocode 9 and by IIW as follows:

1. Select a reference detail with known fatigue resistance from the detail category tables, which is as similar as possible to the detail being assessed with respect to weld quality and to geometric and loading parameters.

   The most similar reference detail for this test set-up is a one sided fillet weld. Detail type 9.3 and category 12-3,4 in Eurocode 9 and structural detail number 5 from IIW is applied.

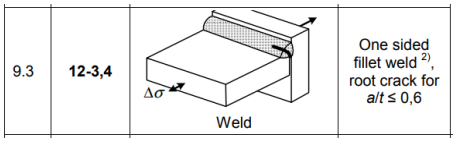

(a) Eurocode 9

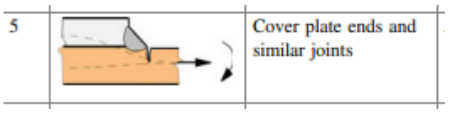

(b) IIW

Figure 18: Detail type and category for the fillet-welded joint between the members.

2. Establish a FEM model of the reference detail and the detail to be assessed with the same type of meshing and elements. Load the reference detail and the detail to be assessed with the stress in which the fatigue resistance is expressed. This is usually nominal stress.

   The process of modeling and conducting finite element analysis on the fillet weld and crane foundation is described in detail in Section 3. The fatigue strength for the used reference detail at $2 \cdot 10^6$ cycles is 12 MPa in Eurocode 9 and 40 MPa in the recommendations from IIW.

3. Determine the hot-spot stress ranges $\Delta\sigma_{HS,ref}$ of the reference detail and the hot-spot stress ranges $\Delta\sigma_{HS,assess}$ of the detail to be assessed. The method for calculating the hot-spot stress is described in Section 1.2.2.

4. The fatigue strength of two million cycles of the detail to be assessed $\Delta\sigma_{C,assess}$ is then calculated from the fatigue class of the reference detail $\Delta\sigma_{C,ref}$ by:

$$\Delta\sigma_{C,assess} = \frac{\sigma_{HS,ref}}{\sigma_{HS,assess}} \Delta\sigma_{C,ref} \tag{14}$$

5. The slope of the S-N curve for the detail to be assessed should be assumed the same m_1 and m_2 as for the reference detail. Using Eurocode 9, the slopes are 3.4 and 5.4 for the selected detail. From IIW, the slopes are 3 and 22.

3 Modeling and Finite Element Analysis

In this chapter, the finite element method is described and an outline of how the finite element models of the reference model and the crane foundation are designed is given. The results from the analysis shall be used to perform a hot-spot stress analysis in order to establish a hot-spot S-N curve. The reference model of a one sided fillet weld is modeled in Abaqus software and the assessed crane foundation is modeled in Autodesk Inventor Professional 2023.

3.1 Finite Element Method

The finite element method (FEM) is a numerical method that can be used for analysing complex structures and solve engineering problems. The method works by dividing the structure into small elements that are connected by nodes. Equilibrium equations are derived for each element from the principle of minimum potential energy or the principle of virtual work. The equations are then assembled into a global matrix system that can be solved for the unknown displacements, stresses, and strains at the nodes. FEM can handle nonlinearities, large deformations, material properties, and boundary conditions that are difficult to analyze by other methods [51].

3.2 Modeling in Abaqus

Abaqus is a finite element analysis (FEA) software that allows modeling and simulation of complex physical phenomena such as structural mechanics, fluid dynamics, heat transfer, etc. Abaqus can be used to solve linear and nonlinear problems, perform static and dynamic analysis, and create interactive and graphical models. When it comes to fatigue analysis, Abaqus can predict the fatigue life of a component based on the material properties and the loading conditions [52].

3.2.1 Creating the model

The solid model of a one sided fillet weld is modelled according to measurements in Appendix B and Eurocode 9 [49]. The plate thicknesses are 30 mm for the crane cylinder and 40 mm for the flange. The weld is included in the Abaqus solid model as the weld toe geometry can affect the stress distribution. The weld toe is often the weakest part of the structure, and its failure can often cause the entire structure to fail. Therefore, accurate modeling of the weld and its behavior is critical for predicting the overall structural response and ensuring the safety of the structure. The weld geometry for the weld connecting the crane cylinder and the flange is shown in Figure 19. The size of the weld is provided from a welding table from Marin Design. As high tensile stresses acts through the plate, an increased fillet weld is used. Hence, the weld toe should be minimum $0.46t_0$, where t_0 is the plate thickness of the thinnest plate. The weld is to be welded with a 50° angle.

S-N curves are divided into categories of whether the weld is load carrying or not. As the weld investigated in this report is a part of a set-up with two flanges that are bolted together and to the crane (see Appendix B), the weld will be in the middle ground of the two categories. However, since the cylinder carries the most load, the model is made with a gap between the flange and the cylinder, which represents a non-load carrying weld between the two components. If one model the flange and the cylinder as being perfectly welded together, then the model would assume that the weld carries the entire load, which is not the case in reality. By including a gap in the model, the fact that there is a small amount of movement allowed between the two components due to the non-load carrying weld is simulated. This will result in a more accurate representation of the actual behavior of the structure under load [53].

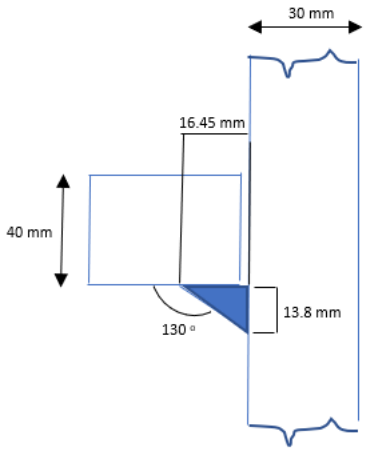

Figure 19: Weld geometry for a 40 mm thick flange welded to a 30 mm thick crane cylinder. The model is made with a 2 mm gap between the flange and the cylinder.

When the elastic strains are small and the material is isotropic, solid models in Abaqus can be modelled with linear-elastic material properties. Linear-elastic material behavior assumes that the material's response is linearly proportional to the applied stresses within the elastic range, and no plastic deformation occurs. This assumption is typically applicable for materials that are expected to resist yielding and plastic deformation under the loading conditions of interest. In the solid model of the weld in Abaqus, linear-elastic material properties are employed, where the Young's modulus is 71000 MPa and the Poisson's ratio is 0.33.

3.2.2 Boundary conditions and load application

The boundary conditions should be set up to accurately represent the loading conditions on the model. As Figure 20 shows, there are applied symmetry boundary conditions for the model. Boundary conditions are applied in all three planes, with the following symmetry:

XY-plane:	z-symmetry
XZ-plane:	y-symmetry
YZ-plane:	x-symmetry

Axial symmetry boundary conditions are applied by constraining the displacements of nodes on the axis of symmetry to be equal and opposite to the displacements of the corresponding nodes on the other side of the axis of symmetry. As the reference model is assumed to be a small part of a larger structure, symmetry along all three axes are assumed.

In the full scale set-up, a crane is attached to the crane foundation. The crane is performing different operations that causes stress in the foundation. As the cylinder is assumed to carry the most load, the load is applied as a uniform pressure over the thickness of the 30 mm thick plate. As the aim is to calculate the hot-spot stress to establish a hot-spot S-N curve, the applied load needs to result in a nominal stress that is 12 MPa orthogonal to the weld according to Eurocode 9 and 40 MPa according to IIW. In an iterative process the needed applied load was found to be -12 N/m (tension) to achieve 12 MPa in nominal stress and -40 N/m to achieve a nominal stress of 40 MPa.

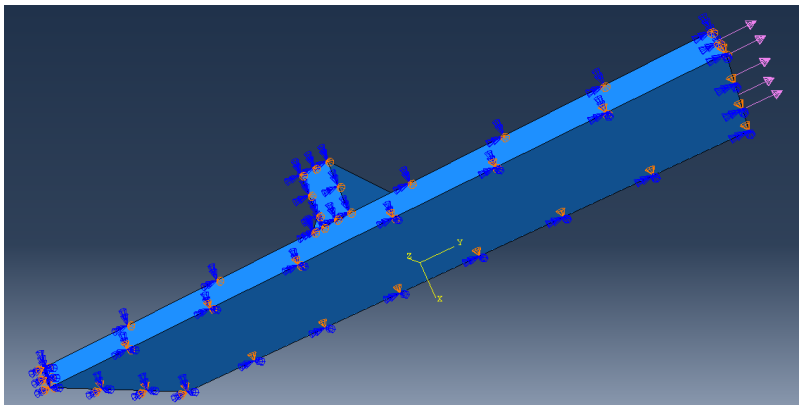

Figure 20: Boundary conditions and load applied to the model in Abaqus

3.2.3 Applying mesh

For the hot-spot analysis, the model was created with quadratic tetrahedral elements, which have higher-order shape functions than the linear tetrahedral elements. This results in a more accurate representation of the displacement and stress fields. Furthermore, these elements are computationally efficient and capable of handling complex geometries. The global mesh size was set to 20 mm. In regions of high stress gradients, such as the weld toe, mesh refinement is often necessary to achieve accurate results. However, in this particular setup, the mesh size in the reference model was kept the same as the assessed model at 20 mm throughout all areas for consistency purposes.

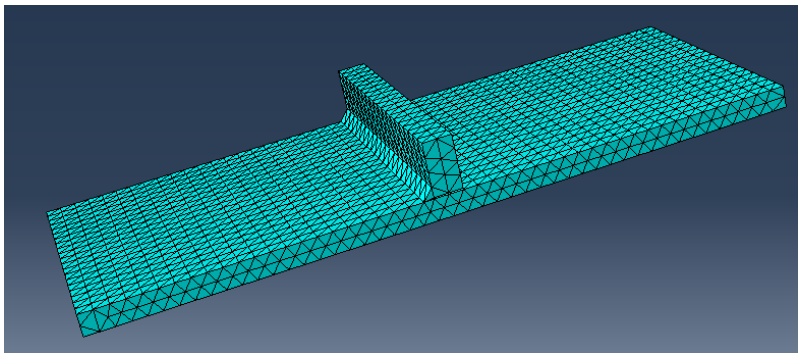

Figure 21: The mesh applied to the model for the hot spot analysis

3.3 Modeling in Autodesk Inventor Professional 2023

Autodesk Inventor Professional is a grade design and engineering software. It is a 3D software that allows the user to design, visualize and simulate products before they are built. Autodesk Inventor Professional includes a finite element analysis (FEA) module that allows users to perform advanced simulations and analysis on their designs. With this module, users can test the structural integrity, thermal behavior, and motion performance of their designs, among other capabilities. The FEA toolset within Inventor Professional provides a wide range of analysis types and options, including linear and nonlinear static analysis, dynamic analysis, and fatigue analysis [54].

3.3.1 Definition of axis system

The axis system that is used is defined in Figure 22. The height is measured along the z-axis of the three dimensional axis system. The axis system is fixed to the vessel. Positive y-axis points towards port side of the vessel, and positive x-axis points forward.

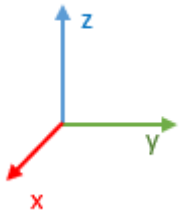

Figure 22: 3D axis system

The point referred to as (x,y,z) = (0,0,0) is indicated with the black arrow ending in a red dot in the element model below:

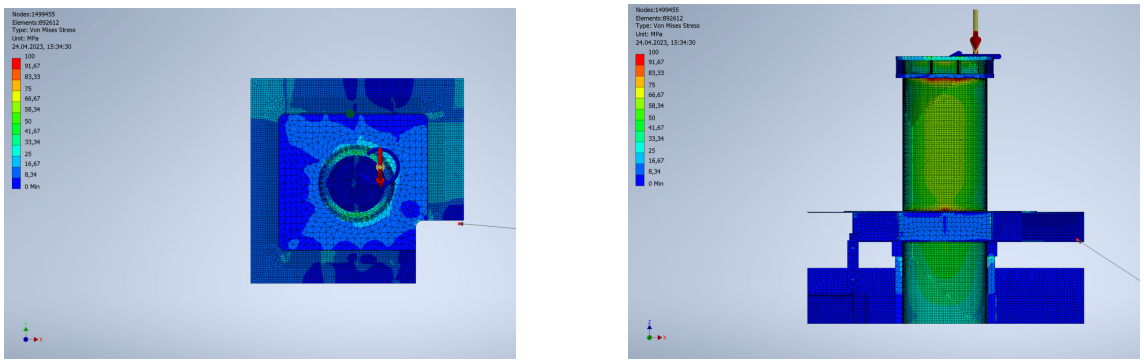

Figure 23: Definition of point (0,0,0) in model in Autodesk Inventor

3.3.2 Creating the model

The finite element model used to assess the crane foundation was provided by Marin Design AS. The model was created according to specific classification rules to ensure that it meets industry standards and regulations. These rules include DNVGL-ST-0342, Section 15.2.1 Craft Version from July 2016, which outlines quality requirements for materials used in the construction of offshore structures [55]. Additionally, DNVGL-RU-HSLC, Part 3, Chapter 3, Section 9, Edition January 2018 which contains requirements for the direct strength calculation and allowable stresses in the structure, was followed [56]. By following these classification rules, the model is able to accurately represent the behavior of the crane foundation and provide reliable results for analysis and evaluation.

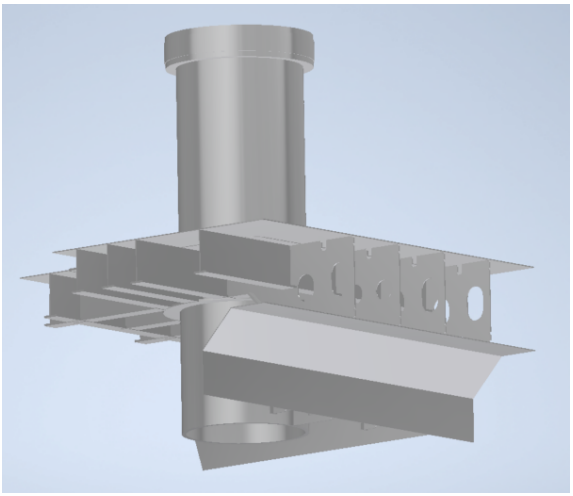

Figure 24: The model of the crane foundation made in Autodesk Inventor Professional is created and provided by Marin Design AS.

3.3.3 Material properties and acceptance criteria

According to DNV-ST-0342. Sec.15.2.1. Craft, the material qualities are as follows:

- Plates: EN AW 5083-H116, material factor for welded plate: f1 = 0.53
- Profiles: EN AW 6082-T6, material factor for welded profile: f1 = 0.48

Table 3 provides information on the material properties of the plates and profiles used in the analyzed structure. The yield strength, ultimate tensile strength, mass density, Young's modulus, Poisson's ratio, and shear modulus for both the plates and profiles are given in the table. This information is essential for finite element analysis, where material properties play a critical role in accurately predicting the behavior of a structure under loading.

	Plates	Profiles
Material type:	EN AW 5083-H116	EN AW 6082 T6
Yield strength:	215 MPa	240 MPa
General Mass density:	2.66 g/cm^3	2.67 g/cm^3
Ultimate Tensile Strength:	305 MPa	290 MPa
Young's Modulus:	71 GPa	69 MPa
Poisson's Ratio:	0.33 ul	0.33 ul
Shear Modulus:	26.00 GPa	25.86 GPa

Table 3: Material properties

The model for both plates and profiles is designed according to the acceptance criteria specified in Table 4. This table outlines the stress requirements that the model must meet. By following these acceptance criteria, the resulting model is able to meet the necessary performance requirements.

	Plates (5083-H116)	Profiles (6082-T6)
Maximum Von Mieses Stress	95.4 MPa	86.4 MPa
Maximum Normal Stress	84.8 MPa	76.8 MPa
Maximum Shear Stress	47.7 MPa	43.2 MPa

Table 4: Acceptance criteria

3.3.4 Boundary conditions

In the finite element model, all elements are represented as solid elements. To ensure a realistic representation of the physical behavior of the structure, boundary conditions must be applied to the model. In this case, all boundaries are fixed in both translational and rotational directions. This means that the structure is completely constrained and cannot move or rotate in any direction, as shown in Figure 25. This setup is often used to simulate structures that are completely fixed to the ground or otherwise completely immobilized, such as some types of supports, anchors, or foundations.

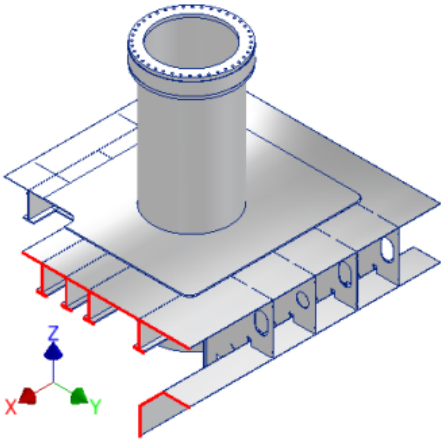

(a) Boundary condition fore

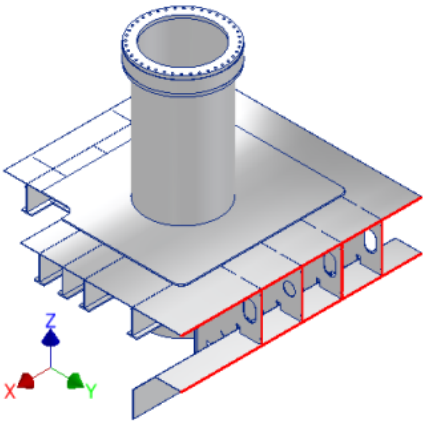

(b) Boundary condition port side

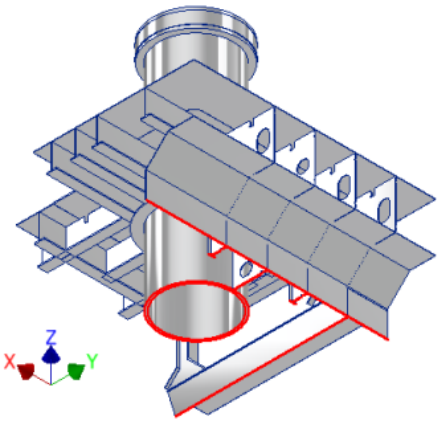

(c) Boundary condition bottom side

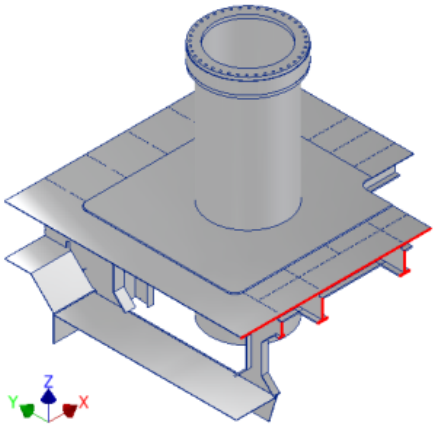

(d) Boundary condition starboard side

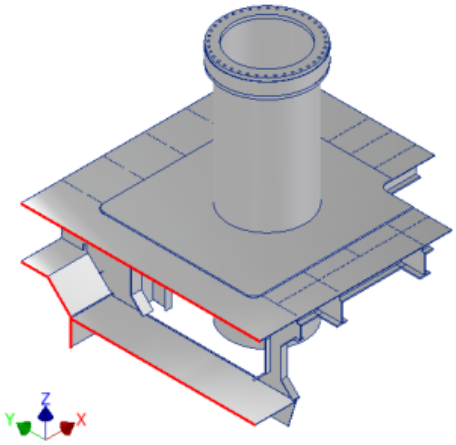

(e) Boundary condition aft side

Figure 25: The boundary conditions applied to the model in Autodesk Inventor.

3.3.5 Application of loads

The structural analysis is performed in a scenario where the load direction are simulated every 45° around the foundation. The load case that provided the worst-case scenario was 90° STB. The design load is given by SWL x dynamic coefficient (ψ). In DNV Craft, a dynamic factor of 1.4 is suggested to include effects from wind, waves etc. [55]. Due to the acceptance criteria, it was decided to use a factor of 1.3 for the finite element analysis, which results in a dynamic moment of 1148 kNm, illustrated by the red arrow in Figure 26. The weight of the crane is 8590 kg and is indicated by the yellow arrow. Gravity is applied to the model by applying a vertical acceleration of g = 9.81 $^{m}/_{s^2}$ to the thick plate (green arrow). The structure is modelled with the element method and has material property aluminium, so that the weight of the structure is considered by the model itself.

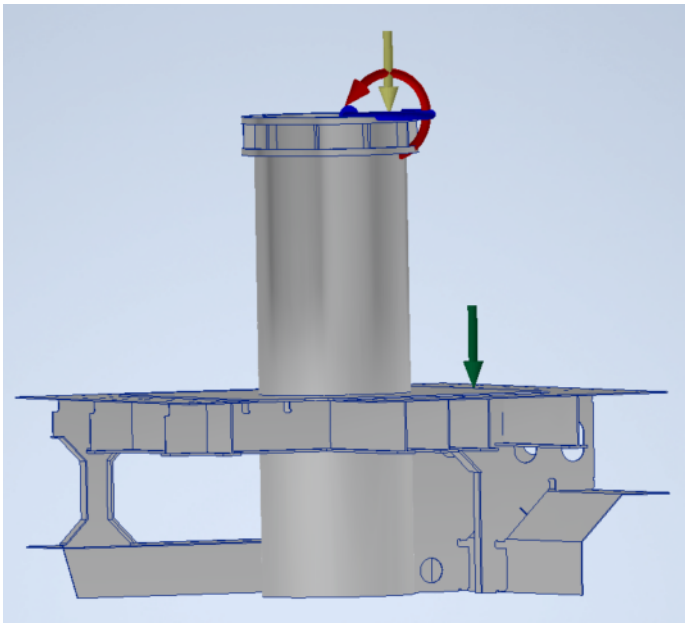

Figure 26: Forces on the foundation

As for the finite element model of the reference model in Abaqus, the nominal stress should be 12 MPa and 40 MPa orthogonal to the weld that is assessed. When the design load is applied to the model, the nominal stress on the port side of the crane foundation was observed to be approximately 75 MPa. Through an iterative process, the required load was determined to be 205 kNm for the nominal stress to be 12 MPa and 620 knm for the nominal stress to be 40 MPa.

3.3.6 Mesh application

The structure is simulated with FEA, using solid tethrahedral elements of at least second order. The mesh set-up, provides the required level of resolution to capture the relevant structural behavior while balancing computational efficiency and accuracy. To create the global mesh, the set-up in Table 5 is used.

Average element size (fraction of model diameter)	0.1
Minimum element size (fraction of average size)	0.2
Gradient factor	1.5
Maximum angle size	60°
Used curved mesh element	Yes
Use part based measure for Assembly mesh	Yes

Table 5: Global mesh set-up

As described, mesh refinement may be necessary in regions of high stress gradients to obtain accurate results. As the weld between the cylinder and the bottom flange is to be assessed and the stress gradient is high in this transition, the mesh is refined on the flange and on the cylinder. The mesh is set to 20 mm to obtain computational efficiency.

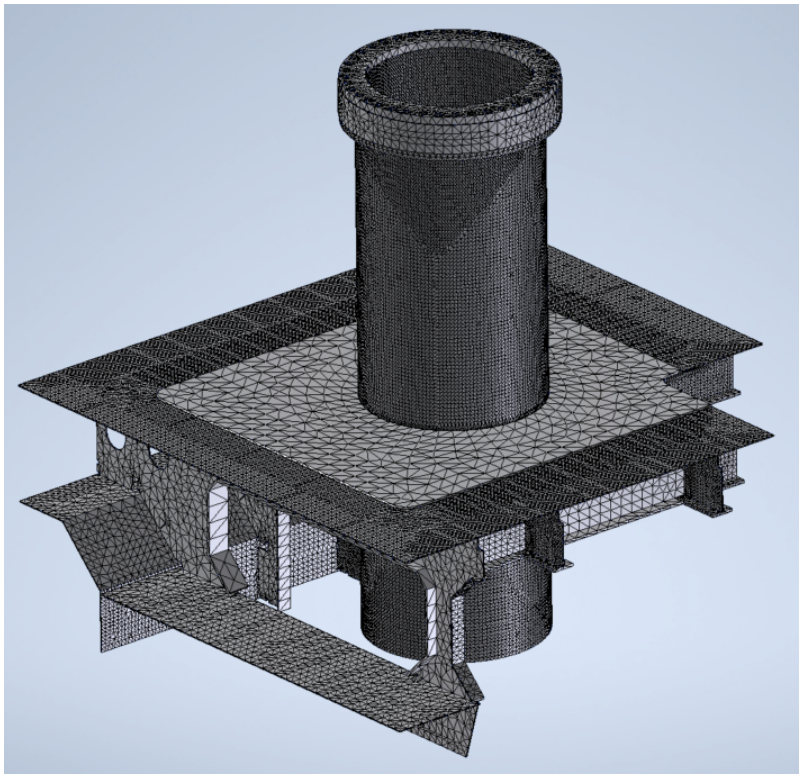

Figure 27: The mesh applied to the solid model for the hot spot analysis.

4 Results

4.1 Hot-spot S-N curve

In this section, two ways of creating the hot-spot S-N curve is described. The first curve is made with fatigue strength data from Eurocode 9, while the second curve is made with data from Recommendations for Fatigue Design of Welded Joints from International Institute of Welding (IIW) [49][17].

4.1.1 Using Eurocode 9 recommendations

In Section 2.3.2, the procedure of calculating the hot-spot S-N curve is described. To determine $\sigma_{HS,ref}$ and $\sigma_{HS,assess}$ finite element models of the reference detail and the detail to be assessed is loaded so the nominal stress is equal to the fatigue strength at $2 \cdot 10^6$ cycles for the reference detail given in Eurocode 9.

Detail type 9.3, category 12-3,4 in Eurocode 9 is the most similar reference detail for the applied test set-up. The fatigue strength at $2 \cdot 10^6$ cycles is 12 MPa and the slopes m_1 and m_2 are 3.4 and 5.4 respectively. The nominal fatigue strength curve is shown in Figure 28.

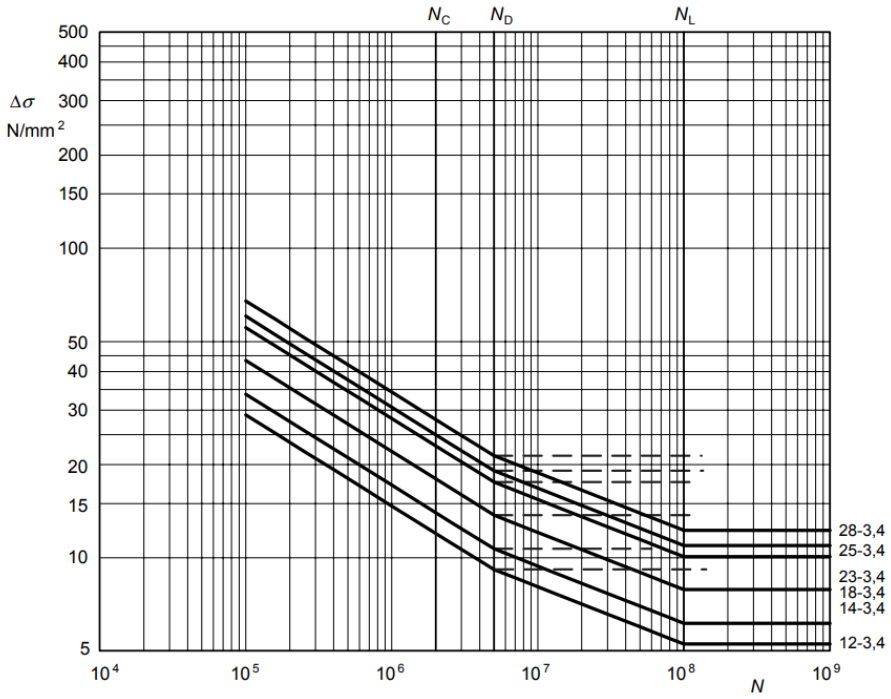

Figure 28: Fatigue strength curves $\Delta\sigma - N$ for fillet-welded joints between members [49].

$\sigma_{HS,ref}$ is determined from the element model made of the reference model in Figure 18a. The modelling procedure is described in Section 3.2. A path is created out from the weld toe as shown in Figure 29a. By plotting the stress that is orthogonal to the weld along the path, the curve in Figure 29c is obtained. The hot-spot stress method is used to calculate the hot-spot stress. The hot-spot stress is determined as the stress at the intersection point of a straight line passing through the stress-curve at a distance of 0.5t and 1.5t from the weld toe with the x-axis at x=0. For this model, the hot-spot stress $\sigma_{HS,ref} = 13.91MPa$.

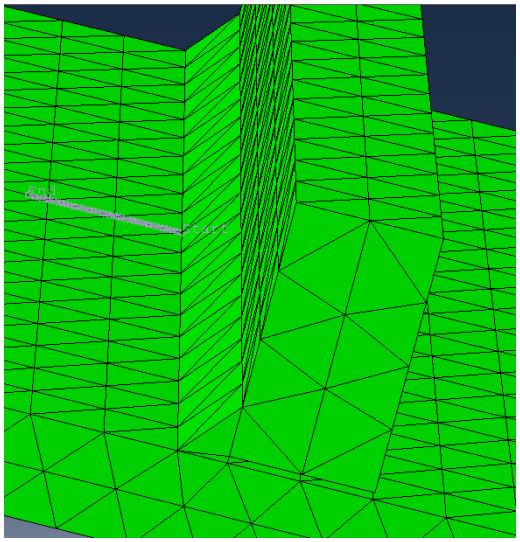

(a) The path is made from the weld toe on top of the plate in the middle of the model.

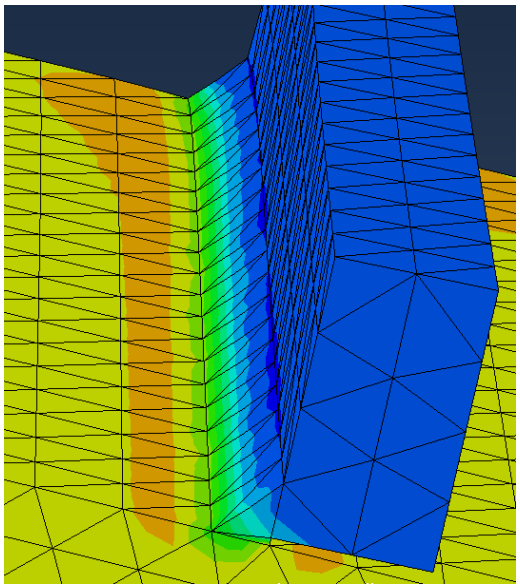

(b) Stress orthogonal to the weld

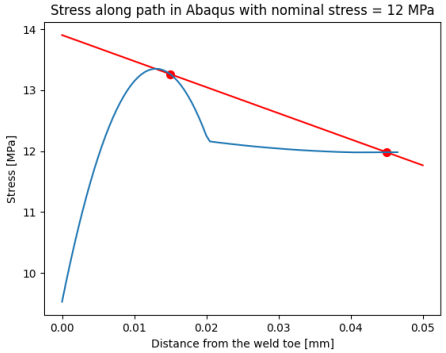

(c) The stress along the path plotted against the distance from the weld toe. The red line is used to calculate the hot-spot stress and intersects through the plotted stress-curve at 0.5t = 15 mm and 1.5t = 45 mm, where t = 30 mm is the thickness of the thinnest plate.

Figure 29: Data used to calculate hot-spot stress for the reference model

$\sigma_{HS,assess}$ is determined from the finite element model of the entire structure that is assessed. The modelling procedure is described in Section 3.3. A path is created out from the weld toe as shown in Figure 30a and the stress orthogonal to the weld along the path is plotted in Figure 30b. Also here, the hot-spot stress is where the red line passes through x=0. The hot-spot stress is found to be $\sigma_{HS,assess} = 17.33MPa$

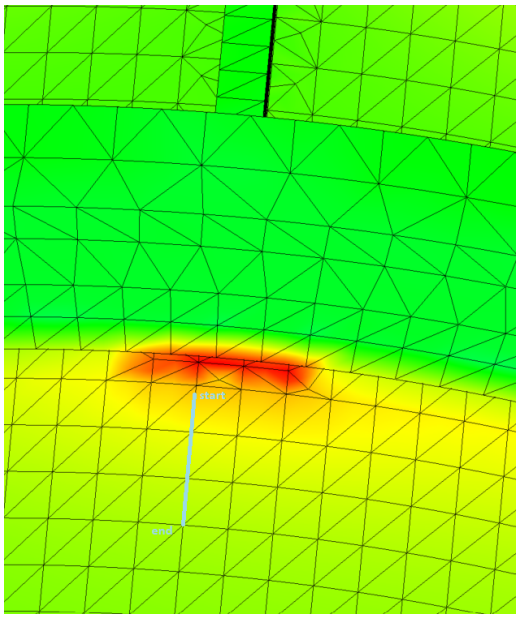

(a) The path is made from the weld toe on port side of the crane cylinder at the point where the stress in orthogonal direction (σ_{zz}) is the most concentrated. The weld is not modelled in inventor, but the weld toe is located 13.8 mm below the flange.

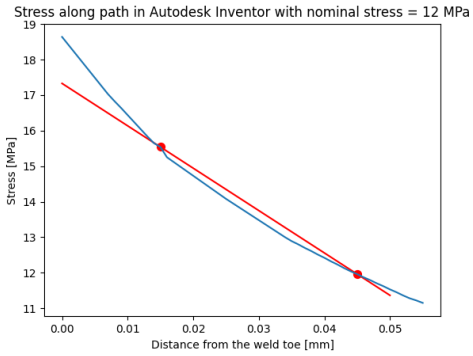

(b) The stress along the path plotted against the distance from the weld toe. The red line is used to calculate the hot-spot stress and intersects through the plotted stress-curve at 0.5t = 15 mm and 1.5t = 45 mm, where t = 30 mm is the thickness of the thinnest plate.

Figure 30: Data used to calculate hot-spot stress for the assessed structure

Lastly, to determine the hot-spot S-N curve, Equation 14 is used with the calculated values:

$$\Delta\sigma_{c,assess} = \frac{13.91MPa}{17.33MPa} \cdot 12MPa = 9.63MPa \tag{15}$$

The calculated value for $\Delta\sigma_{c,assess}$ is the fatigue strength at $2 \cdot 10^6$ cycles for the hot-spot S-N curve. By using this value together with the slopes $m_1 = 3.4$ and $m_2 = 5.4$ the hot-spot S-N curve in Figure 31 is obtained.

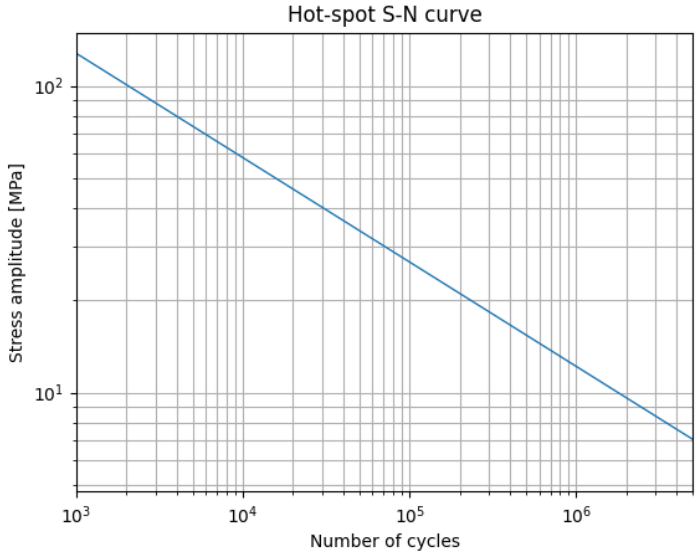

Figure 31: Hot-spot S-N curve for the assessed weld on the crane foundation calculated using recommendations from Eurocode 9.

4.1.2 Using IIW recommendations

When using the recommendations from IIW, with a FAT-value of 40, the stress plotted along the paths for the reference model and the assessed model is given in Figure 32.

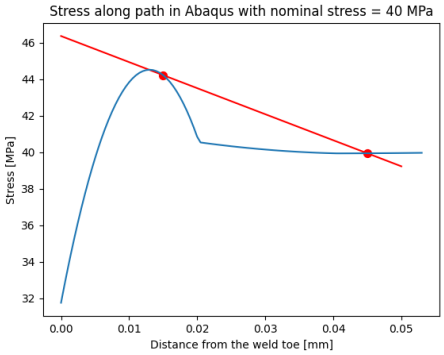

(a) Reference model in Abaqus

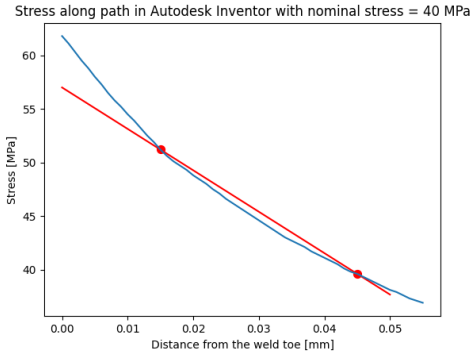

(b) Assessed model in Autodesk Inventor

Figure 32: Stress along path for the reference model and the assessed model, using the same paths as in Section 4.1.1.

The hot-spot stresses are 46.4 MPa and 57.0 MPa for the reference model and the assessed model respectively. The fatigue strength at $2 \cdot 10^6$ cycles in the hot-spot S-N curve for the assessed model is then

$$\Delta\sigma_{c,assess} = \frac{46.4}{57.0} \cdot 40MPa = 32.56MPa \tag{16}$$

Using this value together with the slope $m_1 = 3$ results in the hot-spot S-N curve in Figure 33.

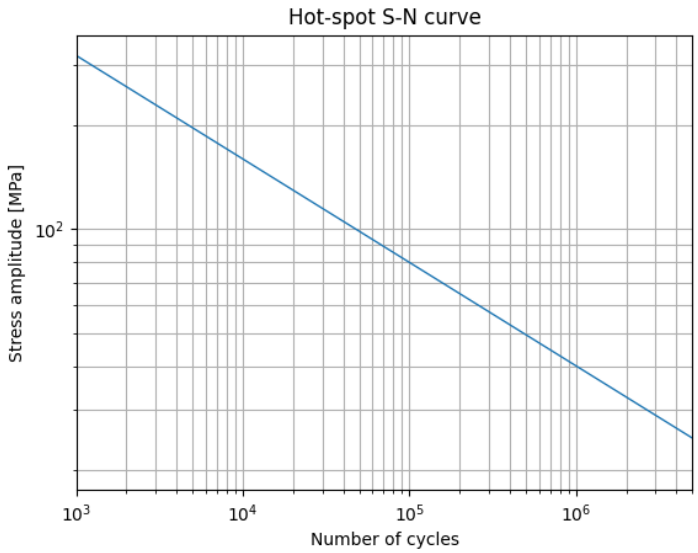

Figure 33: Hot-spot S-N curve for the assessed weld on the crane foundation calculated using recommendations from IIW.

4.2 Ratio between hot-spot stress and stress measured by strain gauges

As the strain gauges are not installed in the area of the hot-spot, the element model in Autodesk Inventor is used to determine the ratio between the hot-spot stress and the stress measured at the location of the strain gauges. As the weld of interest is between the bottom flange and the cylinder, only the ratio between the hot-spot stress and the strain gauge installed orthogonal to the weld inside the crane cylinder is of interest.

As shown in Figure 34, the stress orthogonal to the weld (Stress ZZ) in the location of the strain gauge inside the crane cylinder is 10.41 MPa. The hot-spot stress from the same model was found to be 17.33 MPa. As the material is assumed to act linear-elastic, the ratio between the hot-spot stress and the stress measured by the strain gauge is:

$$ratio = \frac{17.33MPa}{10.41MPa} = 1.66$$

The stress measurements are multiplied by this factor before rainflow counting is carried out.

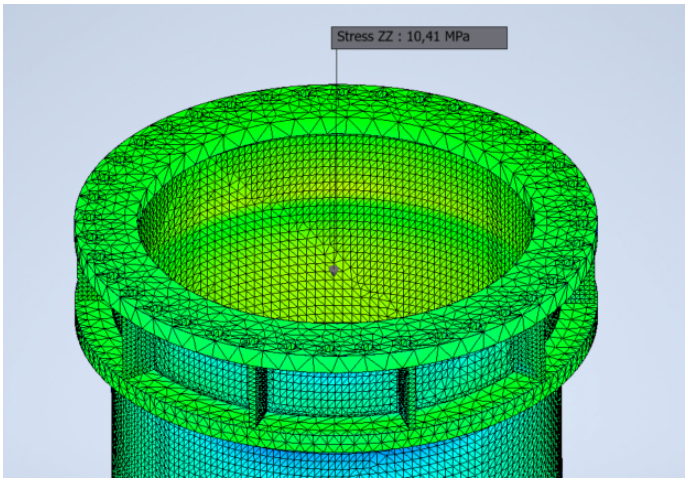

Figure 34: Stress orthogonal to the weld at the location of the strain gauge.

4.3 Measurements

The results from the stress measurements and the pressure transducer are presented in Appendix E. In the left column, the stress measurements from all strain gauges are presented. In the right column, the hot-spot stress at the weld toe of the weld between the flange and the crane cylinder that is calculated by multiplying the stress measured by strain gauge 2 with the ratio between hot-spot stress and stress at the location of the strain gauge is plotted.

It can be seen that the stress measurements from strain gauge 2 is saturated in large parts of the measuring time. Due to this, certain dates are chosen for further fatigue calculations: 1.April, 2.April, 3.April, 22.April, 25.April, 26.April, 29.April, 2.May, 3.May.

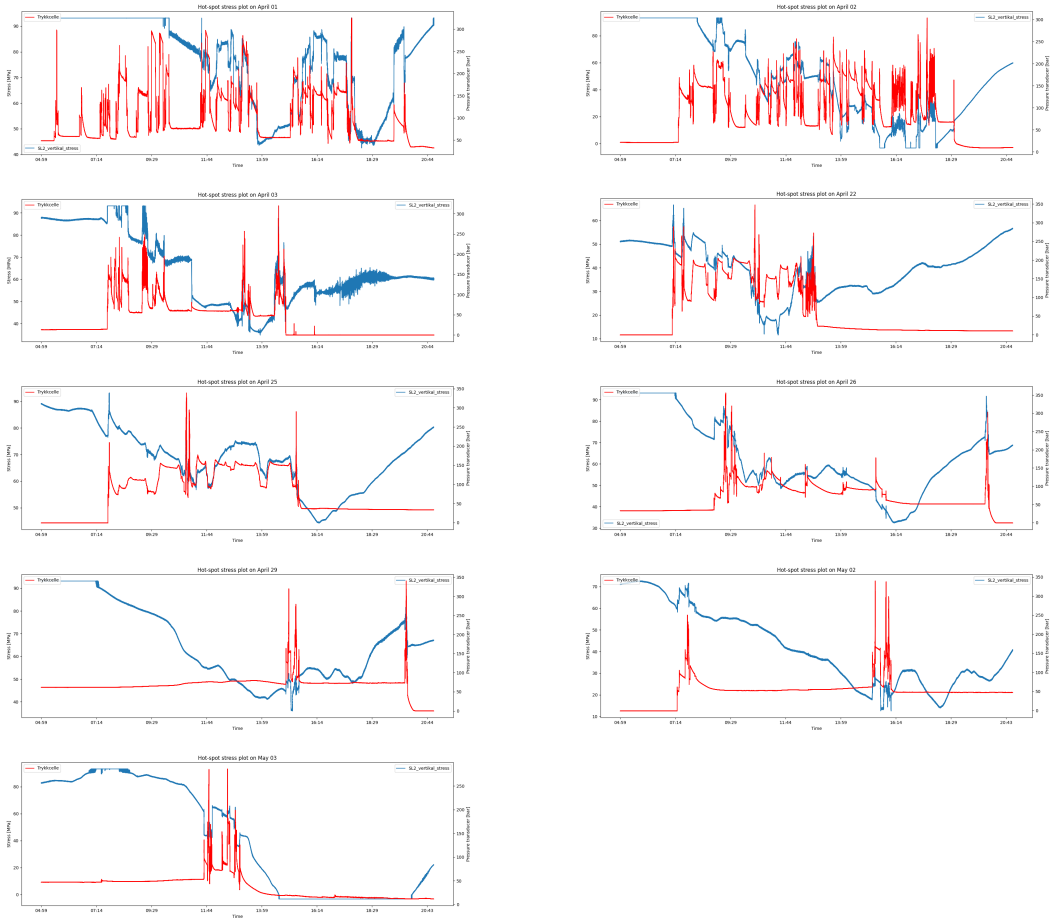

Figure 35: Hot-spot stress calculated from measurements from the vertical strain gauge inside the cylinder on the crane foundation together with pressure in the main cylinder on the crane on 1.April, 2.April, 3.April, 22.April, 25.April, 26.April, 29.April, 2.May and 3.May.

4.4 Fatigue damage

The fatigue damage is calculated using the Palmgren-Miner rule presented in Equation 5. The stress cycles are counted using Rainflow counting with a threshold value. The used threshold values for the calculations are 9 MPa and 32 MPa when using the recommendations from Eurocode 9 and IIW respectively.

The number of cycles to failure for each constant amplitude stress level, along with the cycle count obtained from the measurement data, are provided in Appendix F. The S-N curves shown in Figure 31 and Figure 33 are used to extract the number of cycles to failure.

4.4.1 Recommendations from Eurocode 9

Using the hot-spot S-N curve obtained using recommendations from Eurocode 9, the measurements results in the following fatigue damage

$$D_m = \sum_i \frac{n_i}{N_i} = 0.00258 \tag{17}$$

where D_m is the damage from the measured stress ranges. The fatigue damage value represents the cumulative damage caused by the measured stress ranges. A value of $D = 1$ theoretically

corresponds to failure. With the specific loading profile used in this analysis, the estimated lifespan of the flange on the crane cylinder can be calculated:

$$\frac{1}{D_m} = \frac{1}{0.00251} = 387.6 \tag{18}$$

Since the data used for analysis was collected over a period of 9 days, the estimated fatigue life for the given loading profile is determined by multiplying the calculated lifespan by the duration of data collection. Therefore, the fatigue life for this specific loading profile is calculated as $387.6 \cdot 9 = 3488.5$ days.

4.4.2 Recommendations from IIW

Using the hot-spot S-N curve obtained using recommendations from IIW, the fatigue damage becomes

$$D_m = \sum_i \frac{n_i}{N_i} = 0.0000844 \tag{19}$$

The estimated lifespan is then 11855.3. The fatigue life for the specific loading profile used in the calculation is then $11855 \cdot 9 = 106698$ days.

5 Discussion

5.1 Scope

As presented, the primary objective of this thesis is to determine the fatigue life of the welded flange on the cylinder on the crane foundation of a small service vessel. In Section 4, it was mentioned that the data obtained from strain gauge 2, which is installed vertically in the crane cylinder, is the main focus for the fatigue life calculation. Consequently, unless stated otherwise, the discussion in this section specifically pertains to the measurements obtained from this strain gauge or the corresponding location.

5.2 Finite element analysis of reference and assessed models

In order to determine the hot-spot S-N curve for the assessed welding detail, it was necessary to create finite element models for both the reference detail and the assessed structure. These models served as the foundation for further analysis and calculations.

In the finite element model of the reference detail, a non-load carrying weld is used, which is simulated by introducing a gap between the crane cylinder and the flange. In reality, the weld partially carries the load as the crane is bolted through the two flanges on the cylinder. If a model with a load-carrying weld was employed, it would result in higher stress on the flange and an increased stress in the weld toe. However, since the cylinder experiences the highest stress, it was determined that modeling the weld as non-load carrying is appropriate.

During the finite element analysis of the reference detail with a mesh size of 20 mm, it was observed that the stress concentration did not occur at the weld toe as expected, but instead increased approximately 15 mm away from it, as shown in Figure 29c and Figure 32a. This deviation from the anticipated stress distribution can be attributed to the mesh size used in the analysis. The finite element mesh used in the analysis plays a significant role in capturing the stress distribution accurately. Insufficient mesh density can lead to poor representation of stress gradients and hot-spot regions. To improve the accuracy of the analysis and ensure a reliable representation of stress concentrations, it is recommended to conduct sensitivity studies to identify the most appropriate mesh size [57]. A sensitivity study was, however, not conducted for this model as the procedure for calculating the hot-spot S-N curve says that the same mesh type and elements shall be utilized for both the reference detail and the assessed model [49][17].

In the assessed model, the path from which the hot-spot stress is extracted does not start at the transition between the crane cylinder and the flange because the weld is not modeled. Therefore, the path needs to begin where the weld toe is located in the real-life model, which is 13.8 mm below the flange. From Figure 30b, one can see that the curve representing the stress from the assessed model is as expected. It could be argued that the mesh size in the assessed model could be more refined to obtain even more accurate results. On the other side, the used mesh is $^2/_3$t which is a relatively fine mesh. The selected mesh size strikes a balance between capturing critical stresses accurately and maintaining computational efficiency within the model.

5.3 Calculating the hot-spot S-N curve

To calculate the hot-spot S-N curve for the weld in this thesis, the nominal S-N curve for the reference detail is combined with the hot-spot stress obtained from finite element models of both the reference detail and the assessed structure, as described in Section 2.3.2. The nominal stress is determined at a distance of 1.5t from the weld toe with a target value that corresponds to the fatigue strength at $2 \cdot 10^6$ cycles according to the nominal S-N curve.

The hot-spot stresses obtained from the finite element models were observed to be higher than the nominal stress value. Additionally, the hot-spot stress in the assessed model was found to be greater than that of the reference detail. These findings align with expectations and indicate that

the assessed structure experiences more significant stress concentrations compared to the reference detail.

Two hot-spot S-N curves were calculated, one based on the requirements specified in Eurocode 9 and the other using recommendations provided by the International Institute of Welding (IIW). In Eurocode 9, the fatigue strength from the nominal S-N curve assigned to the assessed detail at $2 \cdot 10^6$ cycles was 12 MPa. When combined with the finite element models, this resulted in a FAT-value of 9.63 MPa for the hot-spot S-N curve. On the other hand, the IIW recommendations suggest a higher nominal stress value of 40 MPa, which yielded a FAT-value of 32.56 MPa for the hot-spot S-N curve. These distinct values result in a notable disparity between the two hot-spot curves, which will be examined and discussed in greater detail.

5.4 Ratio between hot-spot stress and stress measured by strain gauges

The ratio between the hot-spot stress and the stress at the location of the strain gauge is determined using the finite element model of the structure in Autodesk Inventor. In one load-case, the hot-spot stress is 17.33 MPa, with a corresponding nominal stress of 12 MPa. The stress at the strain gauge location is then 10.41 MPa, resulting in a ratio of 1.66 between the two values. It is assumed that the material behaves linear-elastically, meaning that this ratio should remain constant for all stress levels.

To verify this assumption, further investigation is conducted as shown in Table 6. Three different loads are applied: 205 kNm, 620 kNm, and 1148 kNm, corresponding to nominal stresses of 12 MPa, 40 MPa, and 75 MPa, respectively. The load of 1148 kNm represents the design load of the foundation. By analyzing the ratios between the hot-spot stress and the stress at the strain gauge location under these different loads, the consistency of the linear-elastic assumption can be assessed.

Load	Hot-spot stress	Stress at strain gauge position	Ratio
205 kNm	17.33	10.41	1.66
620 kNm	57	34.5	1.65
1148 kNm	107.85	65.2	1.65

Table 6: Ratios between hot-spot stresses and the stress at the location of the strain gauge.

This analysis shows that the ratio between the hot-spot stress and the stress at the strain gauge location remains consistent for different stress levels. This finding supports the assumption that the material follows linear-elastic principles, where the stress ratio remains constant regardless of the applied load. Therefore, the calculated ratios between the hot-spot stress and the stress at the strain gauge location can be confidently used to estimate the stress levels at different loads for the assessed structure. This provides valuable information for assessing the structural integrity and fatigue life of the welding detail.

5.5 Stress measurement system

5.5.1 Installation

The installation of a stress measurement system on the vessel is a critical aspect that directly influences the accuracy and reliability of the collected data. As described, the stress measurement system installed by Urdal Services, utilizing strain gauges from hbm, resistors from Vishay, a pressure transducer of type Efector500 PT5400, and an IMU from Xsens, is a comprehensive and reliable system for capturing stress and related parameters on the vessel. By using high-quality components and following recommended installation and calibration procedures, the system ensures accurate stress data, enabling a more precise analysis of the vessel's structural behavior under operational conditions.

By looking at the results presented in Appendix E one can see that all strain gauges, except from strain gauge 3 is behaving as expected. When the pressure in the crane cylinder increases/decreases the strain in the strain gauge is increased/decreased. However, for strain gauge 3, the behaviour is more unpredictable. The increase and decrease in stress is not predictable and does not follow a trend, as is the case for the other gauges. Thus, one can conclude that there has probably been damage to the strain gauge, or possibly the cabling, during or after installation of the stress measurement system.

5.5.2 Pressure measurements

The pressure transducer that is used measures the flow through the main cylinder on the crane in current [mA]. When transforming the measured signal to pressure, linear behaviour was assumed, with interpolation points where 4mA output from the pressure transducer equals 0 bar and 20mA equals 400 bar. However, it is important to note that in practical scenarios, there can be slight deviations from perfect linearity. To accurately convert the current readings to pressure, one should apply known pressure values to the transducer and record the corresponding current outputs. By collecting a larger number of calibration points, a calibration curve can be generated.

In Section 2.1.4, the procedure for calculating the torque applied to the crane was outlined. However, as Palfinger would not provide either drawings or measurements of the main cylinder on the crane, it was not possible to calculate the torque. The main drawback is then the inability to determine whether the crane is being used in excessively heavy operations. This lack of information prevents us from assessing whether the calculated fatigue life is based on the crane being subjected to heavy usage or if the usage is more moderate in nature.

5.5.3 Stress measurements

The plots in Appendix E shows that the majority of strain gauges behave as expected. When the pressure in the crane increases, there is a change in stress for all gauges (except for strain gauge 3, which was discussed in Section 5.5.1). However, strain gauge 2 exhibits significantly larger variations in stress compared to the other gauges, and the measurements are frequently saturated. The strain gauge saturates to high values during nighttime and low values during daytime. Therefore, it is highly likely that the large, low frequent changes of the stress are primarily caused by temperature differences. The temperature below deck appears to be more stable.

To counteract the variation due to temperature differences a temperature sensor should have been installed, or the strain gauges should have been installed in a half or full Wheatstone bridge. For fatigue calculations, another solution could be to increase the interval for the measurements to capture a larger variety of signals.

5.5.4 Measurements from the IMU

The measurements from the IMU were not incorporated into this thesis. The idea was to combine the IMU data with the pressure readings and the strain measurements to explore the correlation between the sea state and the occurrence of the highest measured stresses. This analysis could particularly provide insights in situations where the measured load exceeds the safe working load (SWL) limit.

The IMU data was left out due to limited accessibility and inability to calculate the applied torque on the crane. Obtaining the necessary data from the IMU proved to be challenging, due to technical constraints and logistical issues. As a result, it was not possible to incorporate the IMU data into the analysis. The absence of data pertaining to torque and the IMU prevented the examination of whether loads exceeding the SWL were being encountered and if the loads exceeded SWL due to peak waves.

5.6 Calculation of fatigue damage

5.6.1 Used data

The strain measurement data selected for the fatigue analysis was based on the criterion that the strain measurements remained within the measurement interval for most of the recorded time. The selection of data will impact the calculation of fatigue life. Choosing data where the strain measurements remain within the measurement interval ensures accurately representation of the operational conditions and loading profile experienced by the crane. This allows for a more reliable estimation of the fatigue life of the component.

Comparing the strain gauge data used for the analysis shown in Figure 35 with the remaining measurements presented in Appendix E, it can be observed that the overall usage of the crane during these specific days was slightly higher than the average usage. This implies that the chosen data captures periods of potentially increased stress levels and higher loading conditions. Consequently, the calculation of the fatigue life may be conservative.

5.6.2 Different standards

The fatigue life was calculated using two different standards: Eurocode 9 and recommendations from the International Institute of Welding (IIW). In Section 2.3.2, the difference between the standards are briefly described.

The fatigue life calculated using recommendations in Eurocode 9, was 3488.5 days which is approximately 9.5 years. Using IIW recommendations, the fatigue life is 106698 days which corresponds to 292 years. The difference between the two are extremely large. The more conservative approach of Eurocode 9 provides a higher level of safety but it also leads to more conservative design requirements. The IIW recommendations, on the other hand, allows for longer fatigue life predictions but require careful consideration of the associated risks and potential limitations. Generally for aluminium structures, different approaches used to calculate the fatigue life results in significant differences in the predicted outcomes. This highlights the influence of methodology and standards on the estimated fatigue life. The variations in factors such as design requirements, safety margins, and assessment methods can lead to contrasting results and interpretations.

6 Conclusion and further work

In conclusion, this strain measurement project has provided valuable insights into the behavior and performance of the studied structure. The installation of strain gauges and the collection of strain data have offered a deeper understanding of the stress distribution and potential fatigue issues. The importance of accurate and reliable strain measurements when assessing the structural integrity of a structure is highlighted. By analyzing the strain data, it was possible to identify areas of high stress concentration and monitor the response of the structure under different loading conditions. The findings of this thesis can be used to improve the design, maintenance, and safety considerations of similar structures.

According to the calculations, Eurocode 9 recommends a fatigue life for the flange in the cylinder of the crane foundation of approximately 9.5 years, whereas the recommendations from IIW indicate a significantly longer fatigue life of 292 years. These variations is attributed to the different approaches and criteria adopted by each standard. Eurocode 9 is the European standard, while IIW gives international recommendations. When designing vessels in Norway, it is crucial to consider regulations and standards applied in this country. In this context, Eurocode 9 serves as a relevant reference for fatigue life estimation and design requirements as its conservative approach aligns with the safety-oriented practices and regulations in the country. As mentioned in the introduction, some vessels have experienced cracks in the weld below the flange on the cylinder on the foundation after much shorter time. As the calculated fatigue life at worst may be 9.5 years it can be concluded that these cracks likely is caused by pore welding, not the material itself.

The collection and analysis of stress data is considered partly successfull as the project encountered certain limitations and challenges. The accessibility of certain data, such as torque measurements and IMU data, proved to be difficult, which restricted certain analysis of the system. Additionally, factors like temperature variations and measurement saturation in certain strain gauges posed challenges in interpreting the results accurately.

The data obtained from this project can serve as a foundation for future investigations and inform decision-making processes in the field of structural engineering. To further research and develop the findings and limitations of this thesis, several areas may be further explored and improved:

1. Extending the data collection: Extending the data collection period to include a larger range of operating conditions, such as varying sea states and load profiles. This would enhance the accuracy and reliability of the fatigue analysis. Additionally, adding more strain gauges or sensors in different locations of the structure could provide an even larger understanding of the stress distribution. To further enhance the accuracy and reliability of strain measurements, advanced techniques and technologies, such as fiber optical strain sensors could also be explored.

2. Calibration and validation: Calibrating the strain gauges so that all measurements are in the measurement interval and validating their measurements against other independent methods or techniques would strengthen the reliability of the collected data. The pressure transducer would also provide more reliable data if a calibration curve was made.

3. Integrate environmental data: Integrating data such as sea state conditions, wind speeds, and vessel motions with the strain gauge measurements would enable a more comprehensive analysis of the effects of these factors on fatigue life.

Other interesting topics worth exploring are how the stress distributes throughout the crane foundation and how corrosion or temperature effects affects the fatigue life. It would also be interesting to conduct comparative studies between different design standards and recommendations, beyond Eurocode 9 and IIW. This would provide a broader understanding of their applicability and limitations.

Bibliography

[1] Eurostat. *Production from aquaculture excluding hatcheries and nurseries (from 2008 onwards)*. 2021. URL: https://ec.europa.eu/eurostat/databrowser/view/fish_aq2a/default/table?lang=en.

[2] Eirik Mikkelsen. *Om norsk havbruksnæring*. 2022. URL: https://www.barentswatch.no/havbruk/havbruksnaring.

[3] Bård Misund. *fiskeoppdrett*. 2022. URL: https://snl.no/fiskeoppdrett.

[4] Bjørnar Skjæran. *The road ahead to a sustainable aquaculture industry in Norway*. Aug. 2022. URL: https://www.innovationnewsnetwork.com/the-road-ahead-to-a-sustainable-aquaculture-industry-in-norway/24698/.

[5] Kystrederiene. *Multifunksjon og service*. URL: https://kystrederiene.no/sektorer/.

[6] Kari Stautland. *Kompetansekrav til kranførere på norske fartøy*. June 2018. URL: https://www.sdir.no/aktuelt/nyheter/kompetansekrav-til-kranforere-pa-norske-fartoy/.

[7] O. Gunes. '5 - Failure modes in structural applications of fiber-reinforced polymer (FRP) composites and their prevention'. In: *Developments in Fiber-Reinforced Polymer (FRP) Composites for Civil Engineering*. Ed. by Nasim Uddin. Woodhead Publishing, 2013. URL: https://www.sciencedirect.com/science/article/pii/B9780857092342500051.

[8] Stig Berge and Sigmund Kyrre Ås. *Compendium - Fatigue and Fracture Design of Marine Structures*. 3rd ed. NTNU - Faculty of Engineering Science and Technologies, 2017.

[9] George Antaki and Ramiz Gilada. 'Chapter 2 - Design Basis Loads and Qualification'. In: *Nuclear Power Plant Safety and Mechanical Integrity*. Ed. by George Antaki and Ramiz Gilada. Boston: Butterworth-Heinemann, 2015, pp. 27–102. URL: https://www.sciencedirect.com/science/article/pii/B9780124172487000023.

[10] Torstein Mann. 'Fatigue assessment methods for welded structures and their application to an aluminium T-joint'. PhD thesis. 2006. URL: https://ntnuopen.ntnu.no/ntnu-xmlui/bitstream/handle/11250/241283/121818_FULLTEXT01.pdf?sequence=1.

[11] Almar Almar-Næss et al. *Basic fatigue properties of welded joints*. Trondheim: Tapir, 1985.

[12] *Eurokode 9: Design of aluminium structures*. NS-EN 1999-1-3:2007+NA:2010. Brüssel: CEN, 2010.

[13] Norman E. Dowling. *Mechanical behavior of materials: engineering methods for deformation, fracture and fatigue*. 4th ed. Boston: Pearson Education, 2013.

[14] Stephen J. Maddox. 'Review of fatigue assessment procedures for welded aluminium structures'. In: *International Journal of Fatigue* 25.12 (2003). URL: https://www.sciencedirect.com/science/article/pii/S014211230300063X.

[15] B. Phelps and B. Morris. *Review of Hull Structural Monitoring Systems for Navy Ships*. Australia: Maritime Platform Division - DSTO Defence Science and Technology Organisation, May 2013. URL: https://apps.dtic.mil/sti/pdfs/ADA588962.pdf.

[16] Wim De Waele Kris Hectors. *Cumulative Damage and Life Prediction Models for High-Cycle Fatigue of Metals: A review*. 2019. URL: https://www.mdpi.com/2075-4701/11/2/204.

[17] A. Hobbacher. *Recommendations for Fatigue Design of Welded Joints and Components*. 2nd ed. New York: Springer International Publishing, 2016.

[18] Yung-Li Lee and Tana Tjhung. 'Chapter 3 - Rainflow Cycle Counting Techniques'. In: *Metal Fatigue Analysis Handbook*. Ed. by Yung-Li Lee, Mark E. Barkey and Hong-Tae Kang. Boston: Butterworth-Heinemann, 2012, pp. 89–114. URL: https://www.sciencedirect.com/science/article/pii/B9780123852045000033.

[19] DNVGL-RP-C203. *Fatigue design of offshore steel structures*. DNV GL, Apr. 2016.

[20] Standards Norway. *NORSOK N-044: Design of steel structures*. Oslo: Norwegian Technology Standards Institution, 2004.

[21] Boris Fuštar, Ivan Lukačević and Darko Dujmović. 'High-Frequency mechanical impact treatment of welded joints'. In: *Gradevinar* (July 2020).

[22] Wikipedia. *Strain gauge*. Oct. 2022. URL: https://en.wikipedia.org/wiki/Strain_gauge.

[23] HBM. *The Wheatstone Bridge Circuit Explained*. URL: https://www.hbm.com/en/7163/wheatstone-bridge-circuit/.

[24] John Blyler. *Fundamentals of Strain Gauge Instrumentation Amplifiers*. Feb. 2021. URL: https://www.designnews.com/electronics/fundamentals-strain-gauge-instrumentation-amplifiers.

[25] Karl Hoffmann. *An Introduction to Stress Analysis and Transducer Design using Strain Gauges*. HBM.

[26] ElectronicTutorials. *Wheatstone Bridge*. URL: https://www.electronics-tutorials.ws/blog/wheatstone-bridge.html.

[27] TransducerTechniques. *Quarter Bridge, Half Bridge and Full Wheatstone Bridge Strain Gauge Load Cell configurations*. URL: https://www.transducertechniques.com/wheatstone-bridge.aspx.

[28] Wikipedia. *Wheatstone Bridge*. Oct. 2022. URL: https://en.wikipedia.org/wiki/Wheatstone_bridge.

[29] mantracourt.com. *LCD20 User Manual*. Mantracourt Electronics Ltd, Mar. 2016.

[30] TacunaSystems. *How Does an Optical Strain Gauge Work?* Mar. 2022. URL: https://tacunasystems.com/knowledge-base/how-does-an-optical-strain-gauge-work/.

[31] Mousumi Majumder et al. 'Fibre Bragg gratings in structural health monitoring - Present status and applications'. In: *Sensors and Actuators A: Physical* 147 (Sept. 2008), pp. 150–164. URL: https://www.sciencedirect.com/science/article/pii/S0924424708002380.

[32] Thomas Kleckers and Bernd Günther. *Optical versus electrical strain gages: A comparison*. July 2007. URL: https://theengineer.markallengroup.com/production/content/uploads/2013/10/HBM24.pdf.

[33] Charles Pao. *Exploring the Application of Gyroscopes*. CEVA, Nov. 2018. URL: https://www.ceva-dsp.com/ourblog/exploring-the-application-of-gyroscopes/.

[34] Maria Martinez-Luengo, Athanasios Kolios and Lin Wang. 'Structural health monitoring of offshore wind turbines: A review through the Statistical Pattern Recognition Paradigm'. In: *Renewable and Sustainable Energy Reviews* 64 (2016), pp. 91–105. URL: https://www.sciencedirect.com/science/article/pii/S1364032116301976.

[35] Vectornav. *MEMS operation*. URL: https://www.vectornav.com/resources/inertial-navigation-primer/theory-of-operation/theory-mems?gclid=CjwKCAiAmuKbBhA2EiwAxQnt7_X5YvqnTd1f7RnO5iFvJbrD5DRtvBwE.

[36] Anders Brandt. *Noise and Vibration Analysis: Dignal Analysis and Experimental Procedures*. A John Wiley and Sons, 2011.

[37] Hongbin Shi et al. 'Effect of sampling rate on the accuracy of strain gage measurement during printed circuit board functional test'. In: *2012 13th International Conference on Electronic Packaging Technology and High Density Packaging*. 2012, pp. 903–908.

[38] David Corminboeuf. 'Calibration of bridge standard for strain gauge bridge amplifier'. In: 17th International Congress of Metrology. 2015. URL: https://cfmetrologie.edpsciences.org/articles/metrology/pdf/2015/01/metrology_metr2015_04004.pdf.

[39] Keith R. Cheatle. *Fundamentals of Test Measurement Instrumentation*. 2006. Chap. Chapter 17: Strain Gauge Calibration. URL: https://www.globalspec.com/reference/62594/203279/Chapter-17-Strain-Gauge-Calibration.

[40] Sjøfartsstyrelsen et al. *Nordic Boat Standard for work boats under 15 meters*. Sjøfartsdirektoratet, 1990.

[41] *Industrial Raspberry Pi - The Revolution Pi*. URL: https://revolutionpi.com/.

[42] Karl Hoffmann. *Practical Hints for the Installation of Strain Gauges*. HBM, 2011. URL: https://ingenioer.au.dk/fileadmin/www.ase.au.dk/Filer/Laboratorier_og_vaerksteder/Instrument_Depotet/Udstyr/Strain_gauges/Practical_Hints_for_the_Installation_of_Strain_Gages.pdf.

[43] HBM. *Measuring With Strain Gauges: How to Prevent Unwanted Temperature Effects on Your Measurement Result*. URL: https://www.hbm.com/en/6725/article-temperature-compensation-of-strain-gauges/.

[44] F. Tegtmeier and M. Peters. *ENCAPSULATION AND UNCERTAINTIES OF STRAIN-GAUGE SENSORS FOR STRESS-MONITORING OF CONSTRUCTIONS*. 2005. URL: https://www.imeko.org/publications/tc3-2005/IMEKO-TC3-2005-030u.pdf.

[45] Miha Hiti. 'Reducing the uncertainty of strain gauge amplifier calibration'. In: *ACTA IMEKO* 6 (Dec. 2017), p. 69. DOI: 10.21014/acta_imeko.v6i4.396.

[46] Alan V. Oppenheim and Alan S. Willsky. *Signals and systems*. 2nd ed. Upper Sadle River, New Jersey: Prentice Hall, 1997.

[47] Jérémy Arpin-Pont et al. 'Methodology for estimating strain gauge measurement biases and uncertainties on isotropic materials'. In: *The Journal of Strain Analysis for Engineering Design* 50 (Jan. 2015), pp. 40–50.

[48] Florida Center for Instructional Technology. *Waves in the Ocean*. 2005. URL: https://fcit.usf.edu/florida/teacher/science/mod2/resources/waves.pdf.

[49] *Eurocode 9: Design of aluminium structures - Part 1-3: Structures susceptible to fatigue*. European Committee for Standardization. NS-EN 1999-1-3:2007+NA:2010. Brussels, Belgium, 2010.

[50] A.F. Hobbacher. 'The new IIW recommendations for fatigue assessment of welded joints and components – A comprehensive code recently updated'. In: *International Journal of Fatigue* 31.1 (2009). Fatigue assessment of welded connections, pp. 50–58. ISSN: 0142-1123. DOI: https://doi.org/10.1016/j.ijfatigue.2008.04.002. URL: https://www.sciencedirect.com/science/article/pii/S0142112308001072.

[51] Ehab Ellobody, Ran Feng and Ben Young. 'Chapter 2 - Review of the General Steps of Finite Element Analysis'. In: *Finite Element Analysis and Design of Metal Structures*. Ed. by Ehab Ellobody, Ran Feng and Ben Young. Boston: Butterworth-Heinemann, 2014, pp. 15–30. URL: https://www.sciencedirect.com/science/article/pii/B9780124165618000020.

[52] *Getting Started with ABAQUS*. 2004.

[53] Prajeet Rajaganesan. 'Modelling, evaluation and assessment of welded joints subjected to fatigue'. Linköping University, Department of Management and Engineering, 2020. URL: https://liu.diva-portal.org/smash/get/diva2:1548553/FULLTEXT01.pdf.

[54] Symetri. *Autodesk Inventor Professional — 3D CAD DESIGN AND ENGINEERING TOOLS*. URL: https://www.symetri.co.uk/products/inventor-professional/.

[55] DNV GL. *Craft*. DNV GL, July 2016.

[56] DNV GL. *RULES FOR CLASSIFICATION*. .Part 3 Hull. DNV GL, Jan. 2018. Chap. 3. Structural design principles.

[57] Ricardo Gasparini. 'Mesh Sensitivity Study for CFD Simulations'. In: *Simscale* (2022). URL: https://www.simscale.com/knowledge-base/mesh-sensitivity-cfd/.

Appendix

A Rainflow counting

The Rainflow counting method is by Lee et al. in the Metal Fatigue Analysis Handbook described as follows [18]:

1. The load history must be rotated so the time axis is pointing downwards and the load history resembles a pagoda roof.
2. A flow of rain is starting at each successive extremum point.
3. The flow is considered to stop, and a cycle is closed when:
   (a) It falls opposite a larger maximum (or smaller minimum) point.
   (b) It meets another flow from above.
   (c) It falls of the roof.
4. The same counted reversals are paired to identify each hysteresis cycle.

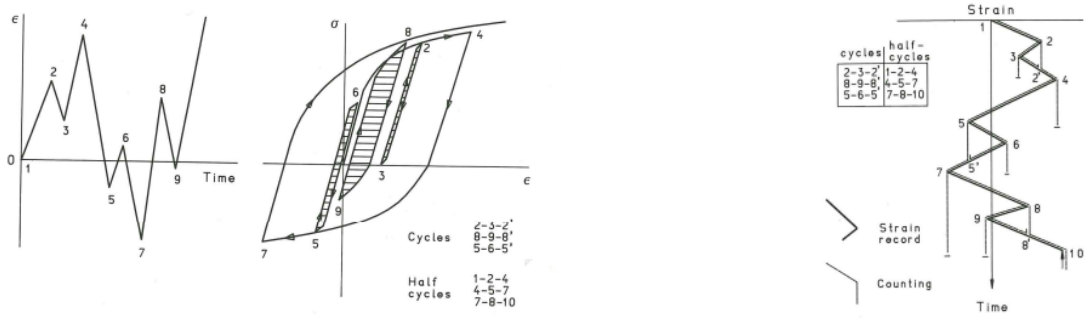

(a) Strain history and corresponding stress-strain response.

(b) Pagoda roof rainflow analogy

Figure 36: Using the rainflow counting method, small cycles within large cycles are counted, similar to the way closed hysteresis loops are formed. The cycle count reflects the way in which the material is responding. [11]

B Crane Foundation Details

Confidential - For Internal Use Only

C Strain gauge locations

Strain Gauge	Direction	X-direction [mm]	Y-direction [mm]	Z-direction [mm]
SL1	Horisontal	-1440	990	1570
SL2	Vertical	-1440	990	1580
SL3	Vertical	-540	560	130
SL4	Horisontal	-540	560	120
SL5	Horisontal	-1425	-225	185
SL6	Vertical	-1425	-225	175
SL7	Horisontal	-2310	560	145
SL8	Vertical	-2310	560	135
SL9	Horisontal	-1430	1175	180
SL10	Vertical	-1430	1175	170

Table 7: Assumed positions of installation of strain gauges

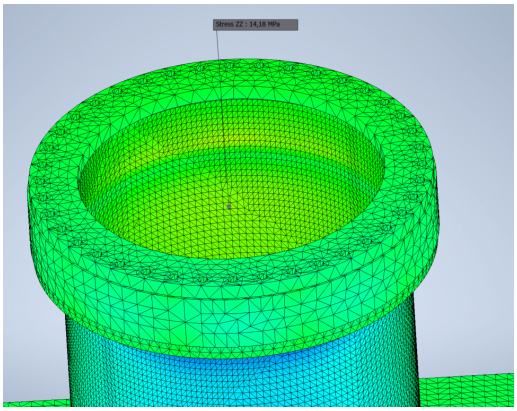

(a) SL1 and SL2

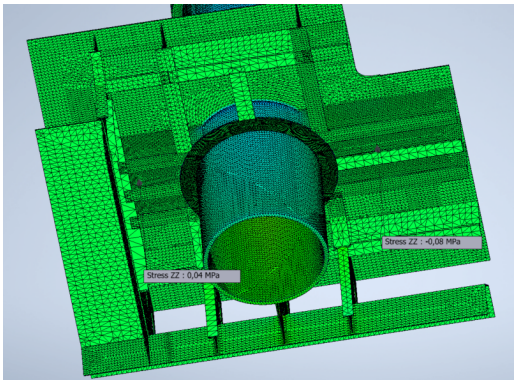

(b) SL3, SL4, SL7 and SL8

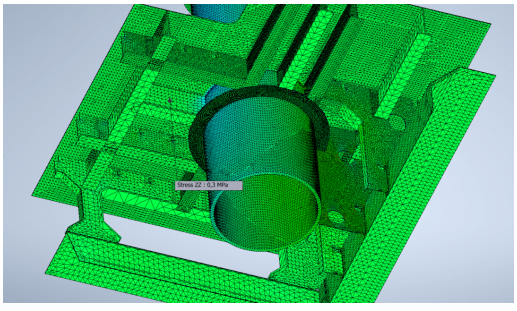

(c) SL5 and SL6

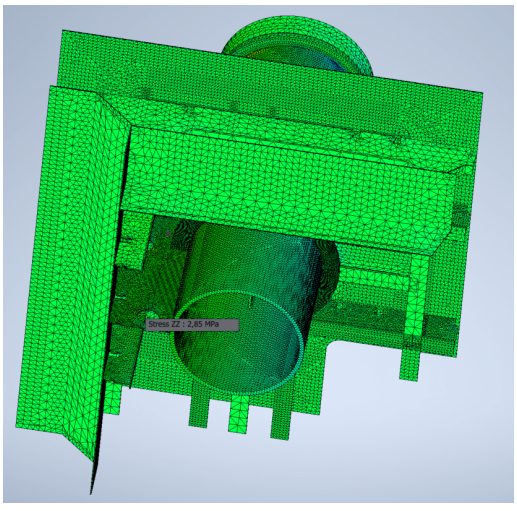

(d) SL9 and SL10

Figure 37: Position of strain gauges together with normal stress in z-direction

D Images of installation points

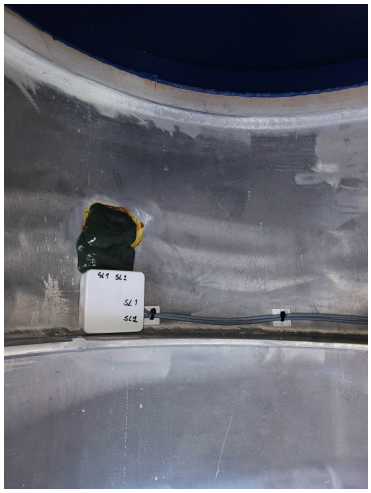

(a) SL1 and SL2 below the flange at starboard side on the inside of the crane cylinder

(b) SL3 and SL4 below deck on the stringer in front of the crane cylinder

(c) SL5 and SL6 below deck on the frame at starboard side of the crane cylinder

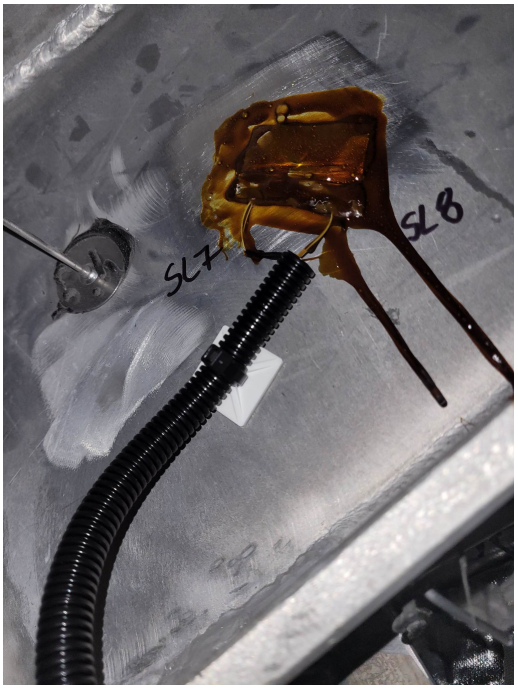

(d) SL7 and SL8 below deck on the stringer aft of the crane cylinder

(e) SL9 and SL10 below deck on port side of the crane cylinder

Figure 38: Installation of strain gauges

E Experimental measurements

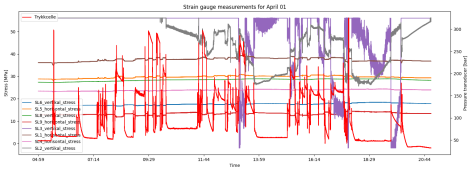

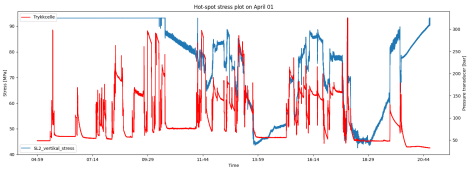

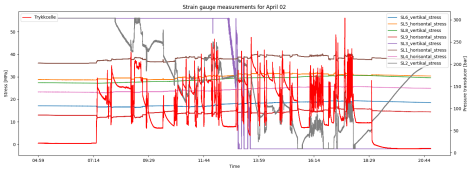

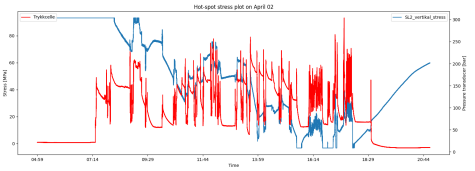

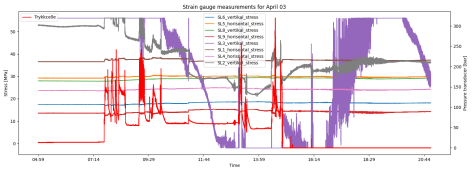

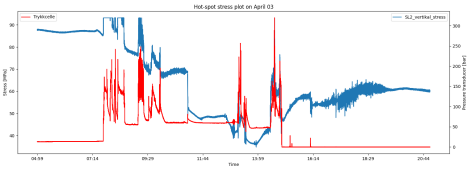

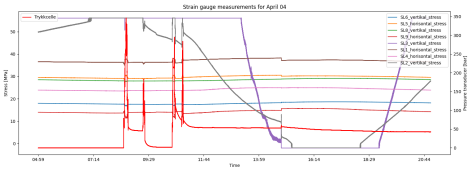

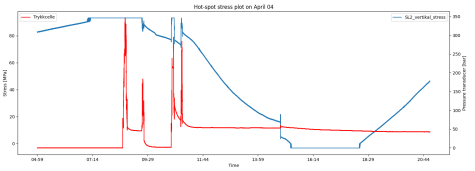

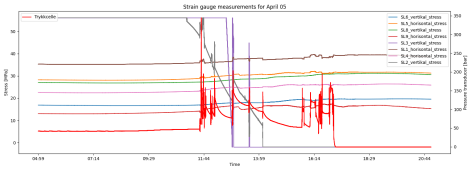

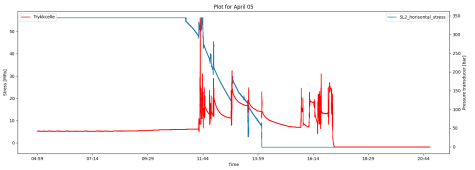

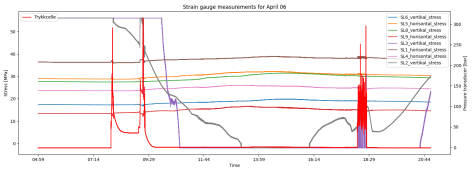

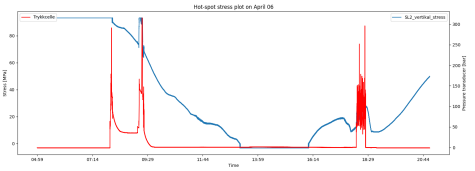

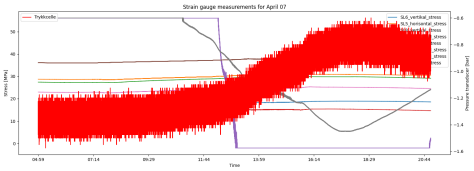

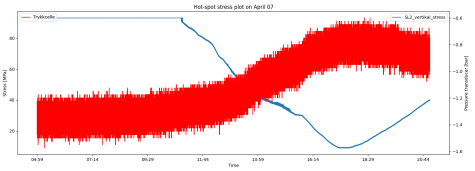

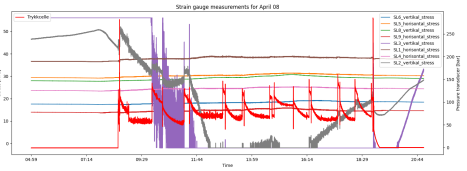
Strain gauge measurements for April 08
Trykkcelle
SL6_vertical_stress
SL5_horisontal_stress
SL8_vertical_stress
SL9_horisontal_stress
SL3_vertical_stress
SL1_horisontal_stress
SL4_horisontal_stress
SL2_vertical_stress
Stress [MPa]
Pressure transducer [bar]
Time

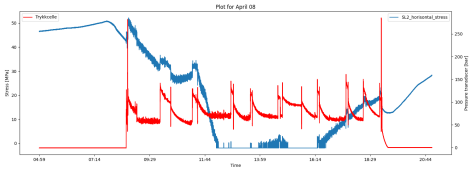
Plot for April 08
Trykkcelle
SL2_horisontal_stress
Stress [MPa]
Pressure transducer [bar]
Time

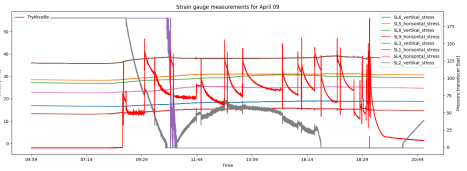
Strain gauge measurements for April 09
Trykkcelle
SL6_vertical_stress
SL5_horisontal_stress
SL8_vertical_stress
SL9_horisontal_stress
SL3_vertical_stress
SL1_horisontal_stress
SL4_horisontal_stress
SL2_vertical_stress
Stress [MPa]
Pressure transducer [bar]
Time

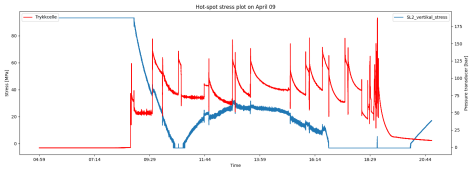
Hot-spot stress plot on April 09
Trykkcelle
SL2_vertical_stress
Stress [MPa]
Pressure transducer [bar]
Time

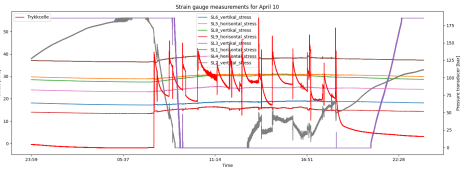
Strain gauge measurements for April 10
Trykkcelle
SL6_vertical_stress
SL5_horisontal_stress
SL8_vertical_stress
SL9_horisontal_stress
SL3_vertical_stress
SL1_horisontal_stress
SL4_horisontal_stress
SL2_vertical_stress
Stress [MPa]
Pressure transducer [bar]
Time

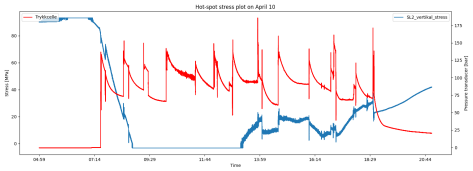
Hot-spot stress plot on April 10
Trykkcelle
SL2_vertical_stress
Stress [MPa]
Pressure transducer [bar]
Time

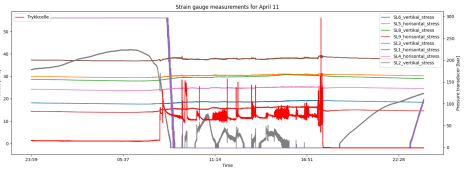
Strain gauge measurements for April 11
Trykkcelle
SL6_vertical_stress
SL5_horisontal_stress
SL8_vertical_stress
SL9_horisontal_stress
SL3_vertical_stress
SL1_horisontal_stress
SL4_horisontal_stress
SL2_vertical_stress
Stress [MPa]
Pressure transducer [bar]
Time

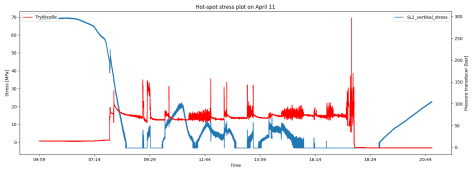
Hot-spot stress plot on April 11
Trykkcelle
SL2_vertical_stress
Stress [MPa]
Pressure transducer [bar]
Time

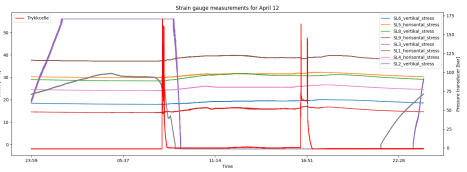
Strain gauge measurements for April 12
Trykkcelle
SL6_vertical_stress
SL5_horisontal_stress
SL8_vertical_stress
SL9_horisontal_stress
SL3_vertical_stress
SL1_horisontal_stress
SL4_horisontal_stress
SL2_vertical_stress
Stress [MPa]
Pressure transducer [bar]
Time

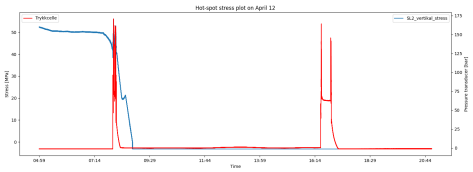
Hot-spot stress plot on April 12
Trykkcelle
SL2_vertical_stress
Stress [MPa]
Pressure transducer [bar]
Time

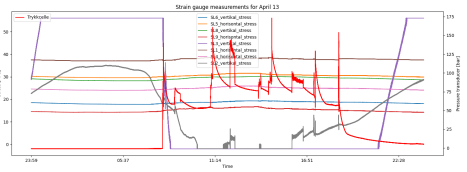
Strain gauge measurements for April 13
Trykkcelle
SL6_vertical_stress
SL5_horisontal_stress
SL8_vertical_stress
SL9_horisontal_stress
SL3_vertical_stress
SL1_horisontal_stress
SL4_horisontal_stress
SL2_vertical_stress
Stress [MPa]
Pressure transducer [bar]
Time

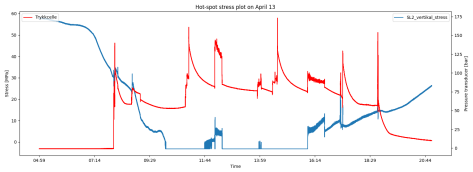
Hot-spot stress plot on April 13
Trykkcelle
SL2_vertical_stress
Stress [MPa]
Pressure transducer [bar]
Time

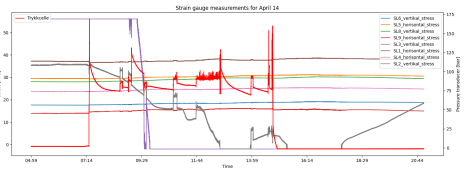
Strain gauge measurements for April 14
Trykkcelle
SL6_vertical_stress
SL5_horisontal_stress
SL8_vertical_stress
SL9_horisontal_stress
SL3_vertical_stress
SL1_horisontal_stress
SL4_horisontal_stress
SL2_vertical_stress
Stress [MPa]
Pressure transducer [bar]
Time

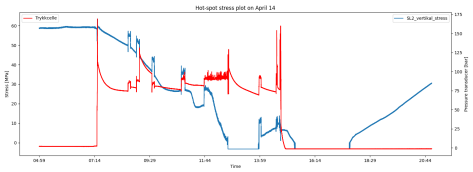
Hot-spot stress plot on April 14
Trykkcelle
SL2_vertical_stress
Stress [MPa]
Pressure transducer [bar]
Time

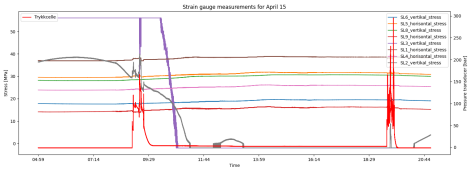
Strain gauge measurements for April 15
Trykkcelle
SL6_vertical_stress
SL5_horizontal_stress
SL8_vertical_stress
SL9_horizontal_stress
SL3_vertical_stress
SL1_horizontal_stress
SL4_horizontal_stress
SL2_vertical_stress
Stress [MPa]
Pressure transducer [bar]
Time

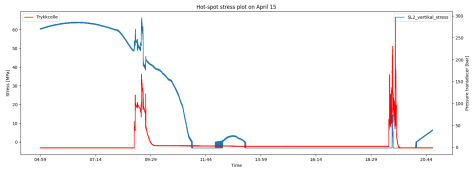
Hot-spot stress plot on April 15
Trykkcelle
SL2_vertical_stress
Stress [MPa]
Pressure transducer [bar]
Time

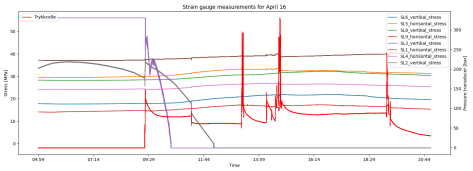
Strain gauge measurements for April 16
Trykkcelle
SL6_vertical_stress
SL5_horizontal_stress
SL8_vertical_stress
SL9_horizontal_stress
SL3_vertical_stress
SL1_horizontal_stress
SL4_horizontal_stress
SL2_vertical_stress
Stress [MPa]
Pressure transducer [bar]
Time

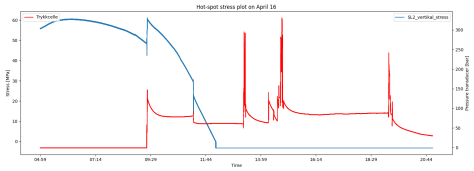
Hot-spot stress plot on April 16
Trykkcelle
SL2_vertical_stress
Stress [MPa]
Pressure transducer [bar]
Time

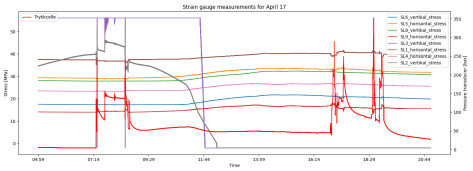
Strain gauge measurements for April 17
Trykkcelle
SL6_vertical_stress
SL5_horizontal_stress
SL8_vertical_stress
SL9_horizontal_stress
SL3_vertical_stress
SL1_horizontal_stress
SL4_horizontal_stress
SL2_vertical_stress
Stress [MPa]
Pressure transducer [bar]
Time

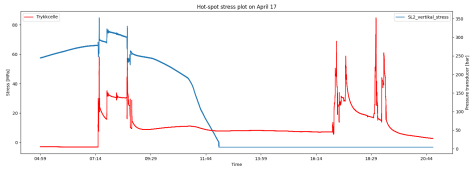
Hot-spot stress plot on April 17
Trykkcelle
SL2_vertical_stress
Stress [MPa]
Pressure transducer [bar]
Time

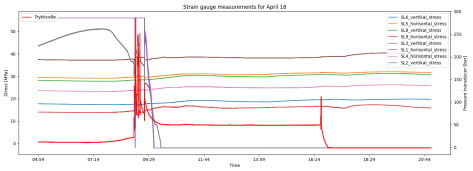
Strain gauge measurements for April 18
Trykkcelle
SL6_vertical_stress
SL5_horizontal_stress
SL8_vertical_stress
SL9_horizontal_stress
SL3_vertical_stress
SL1_horizontal_stress
SL4_horizontal_stress
SL2_vertical_stress
Stress [MPa]
Pressure transducer [bar]
Time

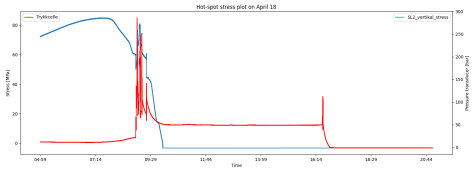
Hot-spot stress plot on April 18
Trykkcelle
SL2_vertical_stress
Stress [MPa]
Pressure transducer [bar]
Time

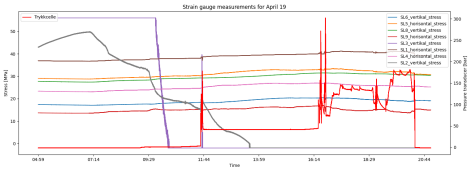
Strain gauge measurements for April 19
Trykkcelle
SL6_vertical_stress
SL5_horizontal_stress
SL8_vertical_stress
SL9_horizontal_stress
SL3_vertical_stress
SL1_horizontal_stress
SL4_horizontal_stress
SL2_vertical_stress
Stress [MPa]
Pressure transducer [bar]
Time

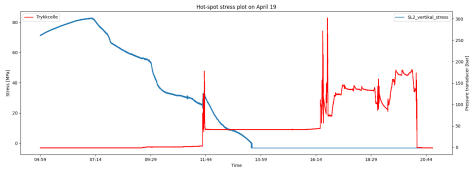
Hot-spot stress plot on April 19
Trykkcelle
SL2_vertical_stress
Stress [MPa]
Pressure transducer [bar]
Time

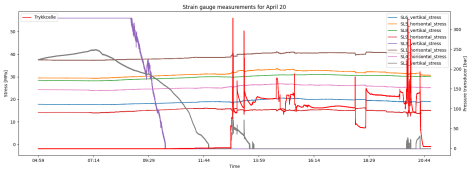
Strain gauge measurements for April 20
Trykkcelle
SL6_vertical_stress
SL5_horizontal_stress
SL8_vertical_stress
SL9_horizontal_stress
SL3_vertical_stress
SL1_horizontal_stress
SL4_horizontal_stress
SL2_vertical_stress
Stress [MPa]
Pressure transducer [bar]
Time

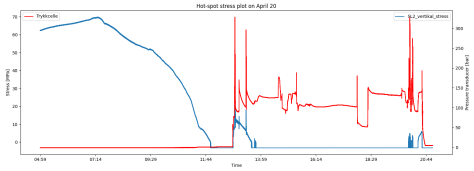
Hot-spot stress plot on April 20
Trykkcelle
SL2_vertical_stress
Stress [MPa]
Pressure transducer [bar]
Time

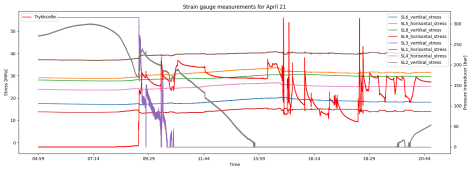
Strain gauge measurements for April 21
Trykkcelle
SL6_vertical_stress
SL5_horizontal_stress
SL8_vertical_stress
SL9_horizontal_stress
SL3_vertical_stress
SL1_horizontal_stress
SL4_horizontal_stress
SL2_vertical_stress
Stress [MPa]
Pressure transducer [bar]
Time

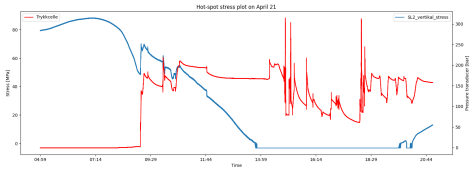
Hot-spot stress plot on April 21
Trykkcelle
SL2_vertical_stress
Stress [MPa]
Pressure transducer [bar]
Time

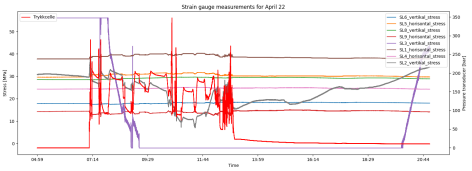
Strain gauge measurements for April 22
Trykkcelle
SL6_vertical_stress
SL5_horisontal_stress
SL8_vertical_stress
SL9_horisontal_stress
SL3_vertical_stress
SL1_horisontal_stress
SL4_horisontal_stress
SL2_vertical_stress
Stress [MPa]
Pressure transducer [bar]
Time

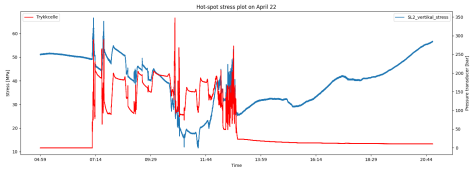
Hot-spot stress plot on April 22
Trykkcelle
SL2_vertical_stress
Stress [MPa]
Pressure transducer [bar]
Time

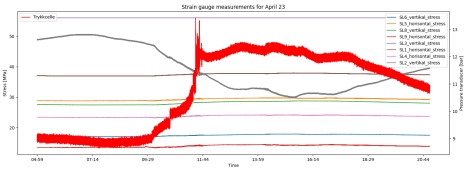
Strain gauge measurements for April 23
Trykkcelle
SL6_vertical_stress
SL5_horisontal_stress
SL8_vertical_stress
SL9_horisontal_stress
SL3_vertical_stress
SL1_horisontal_stress
SL4_horisontal_stress
SL2_vertical_stress
Stress [MPa]
Pressure transducer [bar]
Time

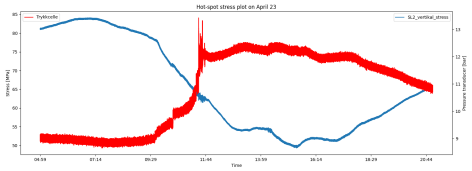
Hot-spot stress plot on April 23
Trykkcelle
SL2_vertical_stress
Stress [MPa]
Pressure transducer [bar]
Time

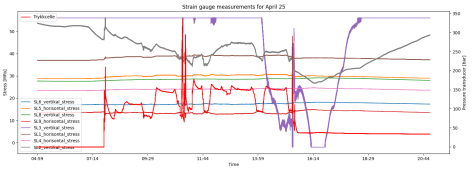
Strain gauge measurements for April 25
Trykkcelle
SL6_vertical_stress
SL5_horisontal_stress
SL8_vertical_stress
SL9_horisontal_stress
SL3_vertical_stress
SL1_horisontal_stress
SL4_horisontal_stress
SL2_vertical_stress
Stress [MPa]
Pressure transducer [bar]
Time

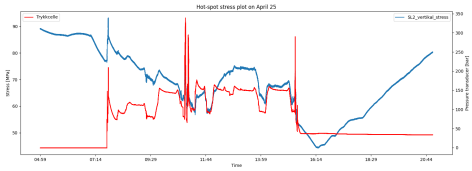
Hot-spot stress plot on April 25
Trykkcelle
SL2_vertical_stress
Stress [MPa]
Pressure transducer [bar]
Time

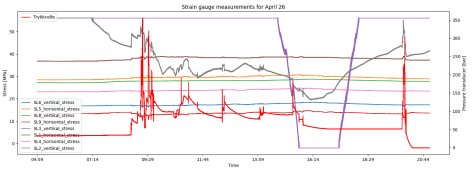
Strain gauge measurements for April 26
Trykkcelle
SL6_vertical_stress
SL5_horisontal_stress
SL8_vertical_stress
SL9_horisontal_stress
SL3_vertical_stress
SL1_horisontal_stress
SL4_horisontal_stress
SL2_vertical_stress
Stress [MPa]
Pressure transducer [bar]
Time

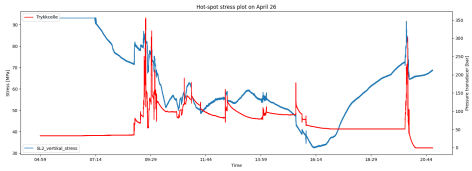
Hot-spot stress plot on April 26
Trykkcelle
SL2_vertical_stress
Stress [MPa]
Pressure transducer [bar]
Time

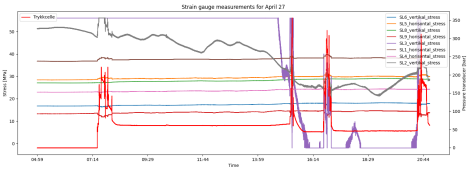
Strain gauge measurements for April 27
Trykkcelle
SL6_vertical_stress
SL5_horisontal_stress
SL8_vertical_stress
SL9_horisontal_stress
SL3_vertical_stress
SL1_horisontal_stress
SL4_horisontal_stress
SL2_vertical_stress
Stress [MPa]
Pressure transducer [bar]
Time

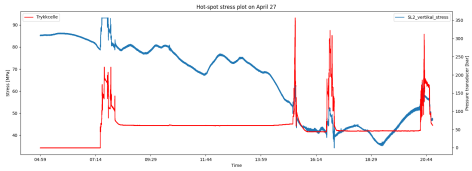
Hot-spot stress plot on April 27
Trykkcelle
SL2_vertical_stress
Stress [MPa]
Pressure transducer [bar]
Time

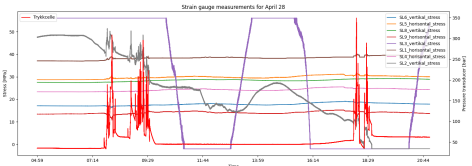
Strain gauge measurements for April 28
Trykkcelle
SL6_vertical_stress
SL5_horisontal_stress
SL8_vertical_stress
SL9_horisontal_stress
SL3_vertical_stress
SL1_horisontal_stress
SL4_horisontal_stress
SL2_vertical_stress
Stress [MPa]
Pressure transducer [bar]
Time

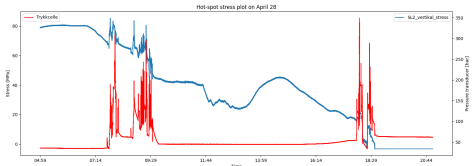
Hot-spot stress plot on April 28
Trykkcelle
SL2_vertical_stress
Stress [MPa]
Pressure transducer [bar]
Time

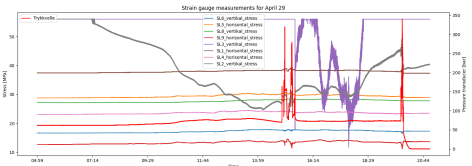
Strain gauge measurements for April 29
Trykkcelle
SL6_vertical_stress
SL5_horisontal_stress
SL8_vertical_stress
SL9_horisontal_stress
SL3_vertical_stress
SL1_horisontal_stress
SL4_horisontal_stress
SL2_vertical_stress
Stress [MPa]
Pressure transducer [bar]
Time

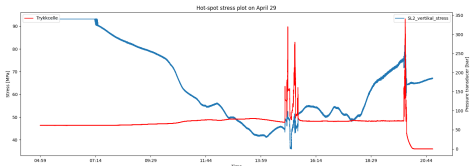
Hot-spot stress plot on April 29
Trykkcelle
SL2_vertical_stress
Stress [MPa]
Pressure transducer [bar]
Time

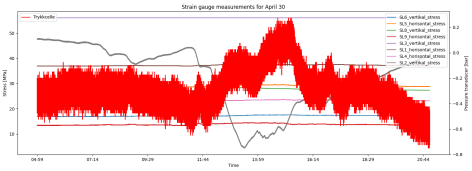
Strain gauge measurements for April 30
Trykkcelle
SL0_vertical_stress
SL5_horisontal_stress
SL8_vertical_stress
SL5_horisontal_stress
SL3_vertical_stress
SL1_horisontal_stress
SL4_horisontal_stress
SL2_vertical_stress
Stress [MPa]
Pressure transducer [bar]
Time

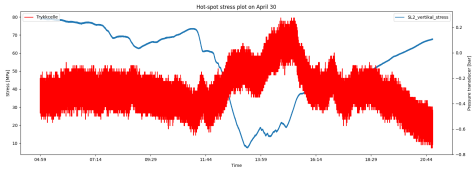
Hot-spot stress plot on April 30
Trykkcelle
SL2_vertical_stress
Stress [MPa]
Pressure transducer [bar]
Time

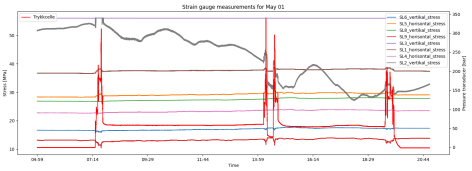
Strain gauge measurements for May 01
Trykkcelle
SL0_vertical_stress
SL5_horisontal_stress
SL8_vertical_stress
SL5_horisontal_stress
SL3_vertical_stress
SL1_horisontal_stress
SL4_horisontal_stress
SL2_vertical_stress
Stress [MPa]
Pressure transducer [bar]
Time

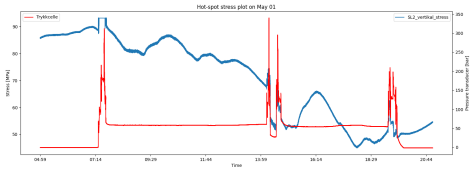
Hot-spot stress plot on May 01
Trykkcelle
SL2_vertical_stress
Stress [MPa]
Pressure transducer [bar]
Time

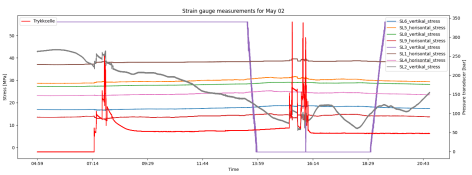
Strain gauge measurements for May 02
Trykkcelle
SL0_vertical_stress
SL5_horisontal_stress
SL8_vertical_stress
SL5_horisontal_stress
SL3_vertical_stress
SL1_horisontal_stress
SL4_horisontal_stress
SL2_vertical_stress
Stress [MPa]
Pressure transducer [bar]
Time

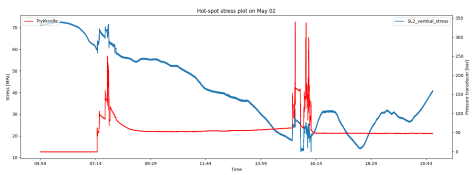
Hot-spot stress plot on May 02
Trykkcelle
SL2_vertical_stress
Stress [MPa]
Pressure transducer [bar]
Time

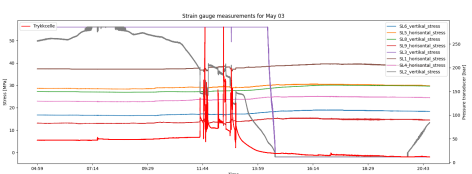
Strain gauge measurements for May 03
Trykkcelle
SL0_vertical_stress
SL5_horisontal_stress
SL8_vertical_stress
SL5_horisontal_stress
SL3_vertical_stress
SL1_horisontal_stress
SL4_horisontal_stress
SL2_vertical_stress
Stress [MPa]
Pressure transducer [bar]
Time

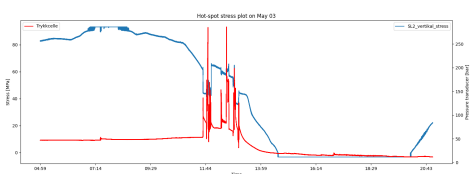
Hot-spot stress plot on May 03
Trykkcelle
SL2_vertical_stress
Stress [MPa]
Pressure transducer [bar]
Time

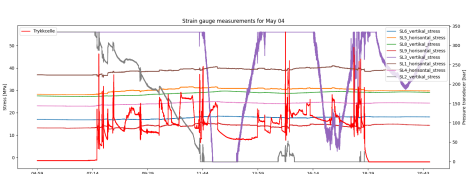
Strain gauge measurements for May 04
Trykkcelle
SL0_vertical_stress
SL5_horisontal_stress
SL8_vertical_stress
SL5_horisontal_stress
SL3_vertical_stress
SL1_horisontal_stress
SL4_horisontal_stress
SL2_vertical_stress
Stress [MPa]
Pressure transducer [bar]
Time

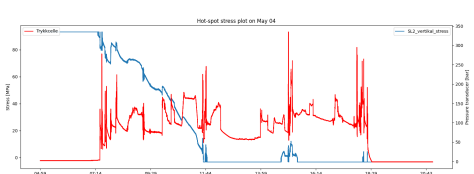
Hot-spot stress plot on May 04
Trykkcelle
SL2_vertical_stress
Stress [MPa]
Pressure transducer [bar]
Time

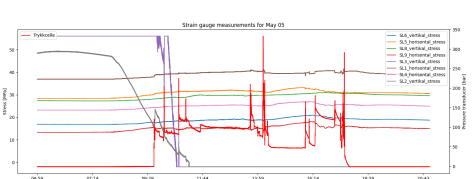
Strain gauge measurements for May 05
Trykkcelle
SL0_vertical_stress
SL5_horisontal_stress
SL8_vertical_stress
SL5_horisontal_stress
SL3_vertical_stress
SL1_horisontal_stress
SL4_horisontal_stress
SL2_vertical_stress
Stress [MPa]
Pressure transducer [bar]
Time

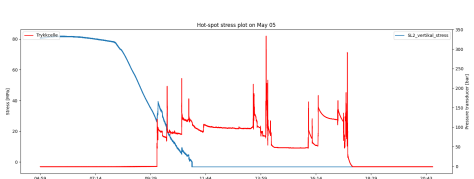
Hot-spot stress plot on May 05
Trykkcelle
SL2_vertical_stress
Stress [MPa]
Pressure transducer [bar]
Time

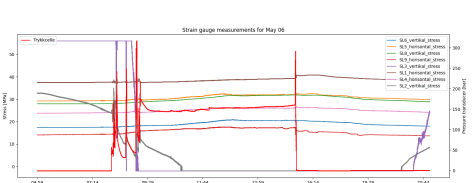
Strain gauge measurements for May 06
Trykkcelle
SL0_vertical_stress
SL5_horisontal_stress
SL8_vertical_stress
SL5_horisontal_stress
SL3_vertical_stress
SL1_horisontal_stress
SL4_horisontal_stress
SL2_vertical_stress
Stress [MPa]
Pressure transducer [bar]
Time

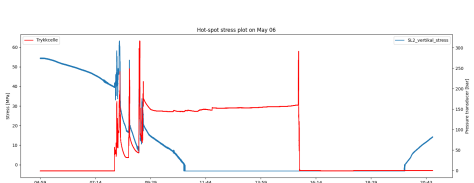
Hot-spot stress plot on May 06
Trykkcelle
SL2_vertical_stress
Stress [MPa]
Pressure transducer [bar]
Time

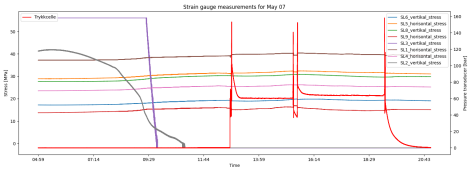
Strain gauge measurements for May 07
Trykkcelle
SL6_vertical_stress
SL5_horizontal_stress
SL8_vertical_stress
SL9_horizontal_stress
SL3_vertical_stress
SL1_horizontal_stress
SL4_horizontal_stress
SL2_vertical_stress
Stress [MPa]
Pressure transducer [bar]
Time

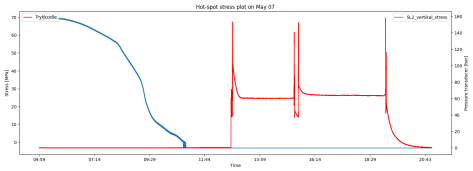
Hot-spot stress plot on May 07
Trykkcelle
SL2_vertical_stress
Stress [MPa]
Pressure transducer [bar]
Time

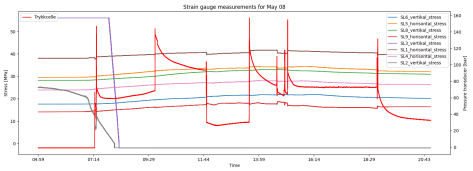
Strain gauge measurements for May 08
Trykkcelle
SL6_vertical_stress
SL5_horizontal_stress
SL8_vertical_stress
SL9_horizontal_stress
SL3_vertical_stress
SL1_horizontal_stress
SL4_horizontal_stress
SL2_vertical_stress
Stress [MPa]
Pressure transducer [bar]
Time

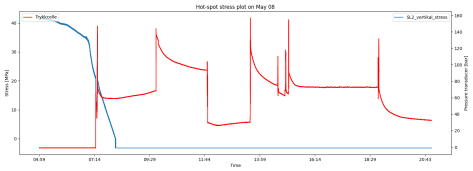
Hot-spot stress plot on May 08
Trykkcelle
SL2_vertical_stress
Stress [MPa]
Pressure transducer [bar]
Time


Strain gauge measurements for May 09
Trykkcelle
SL6_vertical_stress
SL5_horizontal_stress
SL8_vertical_stress
SL9_horizontal_stress
SL3_vertical_stress
SL1_horizontal_stress
SL4_horizontal_stress
SL2_vertical_stress
Stress [MPa]
Pressure transducer [bar]
Time


Hot-spot stress plot on May 09
Trykkcelle
SL2_vertical_stress
Stress [MPa]
Pressure transducer [bar]
Time

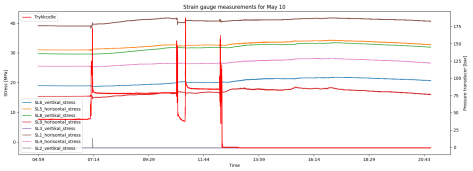
Strain gauge measurements for May 10
Trykkcelle
SL6_vertical_stress
SL5_horizontal_stress
SL8_vertical_stress
SL9_horizontal_stress
SL3_vertical_stress
SL1_horizontal_stress
SL4_horizontal_stress
SL2_vertical_stress
Stress [MPa]
Pressure transducer [bar]
Time

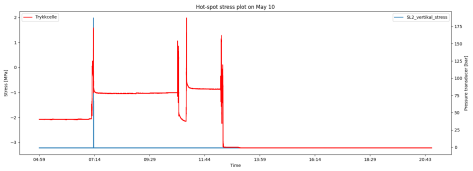
Hot-spot stress plot on May 10
Trykkcelle
SL2_vertical_stress
Stress [MPa]
Pressure transducer [bar]
Time

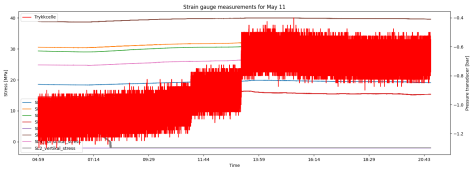
Strain gauge measurements for May 11
Trykkcelle
SL7_vertical_stress
Stress [MPa]
Pressure transducer [bar]
Time

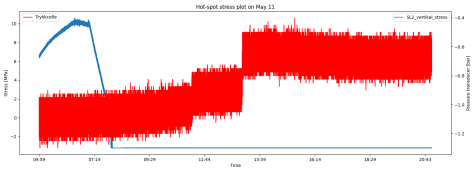
Hot-spot stress plot on May 11
Trykkcelle
SL2_vertical_stress
Stress [MPa]
Pressure transducer [bar]
Time

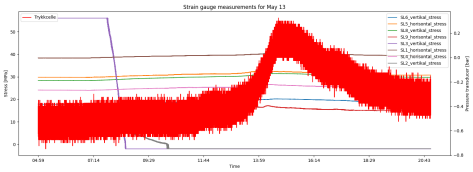
Strain gauge measurements for May 13
Trykkcelle
SL6_vertical_stress
SL5_horizontal_stress
SL8_vertical_stress
SL9_horizontal_stress
SL3_vertical_stress
SL1_horizontal_stress
SL4_horizontal_stress
SL2_vertical_stress
Stress [MPa]
Pressure transducer [bar]
Time

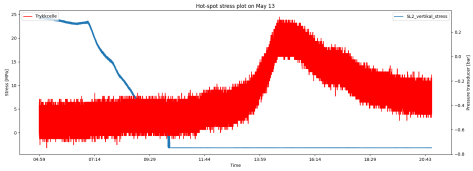
Hot-spot stress plot on May 13
Trykkcelle
SL2_vertical_stress
Stress [MPa]
Pressure transducer [bar]
Time

F Cycle counting

Stress	1. April	2.April	3.Apri	22.April	25.April	26.April	29.April	2.May	3.May	Sum	Cycles to failure	
											Eurocode 9	IIW
9.0 MPa	1	4	10	1	2	1		1	1	21	2440356	
10.0 MPa		3	6	3						12	1790103	
11.0 MPa	1	2	3			1	1	1	2	11	1352474	
12.0 MPa	3	8	5	1	1	1				19	1047106	
13.0 MPa	1	3	3	3	2	1			1	11	827465	
14.0 MPa	2	1	1					1		5	665404	
15.0 MPa		2	1	3	1			1		8	543198	
16.0 MPa		2	1	1		1			1	6	449288	
17.0 MPa	2	1	1		1					5	375910	
18.0 MPa	1	1				1		1		4	317741	
21.0 MPa	2	1	1							4	201917	
22.0 MPa	1	1	1				1			4	176096	
24.0 MPa			1							1	136335	
25.0 MPa	1	1							1	3	120910	
26.0 MPa	1	1							1	3	107738	
27.0 MPa	1	1				1				3	96419	
28.0 MPa				1				1		2	86637	
30.0 MPa	1									1	70725	
31.0 MPa		1								1	64224	
34.0 MPa		1								1	48944	1731353
35.0 MPa	1									1	44944	1571893
36.0 MPa					1					1	41371	1430997
40.0 MPa		1								1	30347	1007191
42.0 MPa		1								1	26290	856024
44.0 MPa	1									1	22928	733064
45.0 MPa		1		1						2	21462	680157
46.0 MPa							1			1	20118	632108
49.0 MPa					1					1	16707	512071
50.0 MPa	1									1	15743	478722
51.0 MPa	1									1	14852	448141
52.0 MPa			1							1	14028	420052
55.0 MPa				1						1	11894	348421
57.0 MPa							1			1	10708	309311
58.0 MPa			2							2	10174	291893
59.0 MPa						1				1	9675	275726
60.0 MPa								1		1	9209	260703
61.0 MPa						1				1	8772	246727
63.0 MPa		1								1	7978	221571
96.0 MPa		1							1	2	2311	54418

Table 8: Results from rainflow counting of the stress measurements on the given dates from strain gauge SL2 in vertical direction inside the crane cylinder together with the number of cycles to failure given from the SN-curve for the different stress ranges.

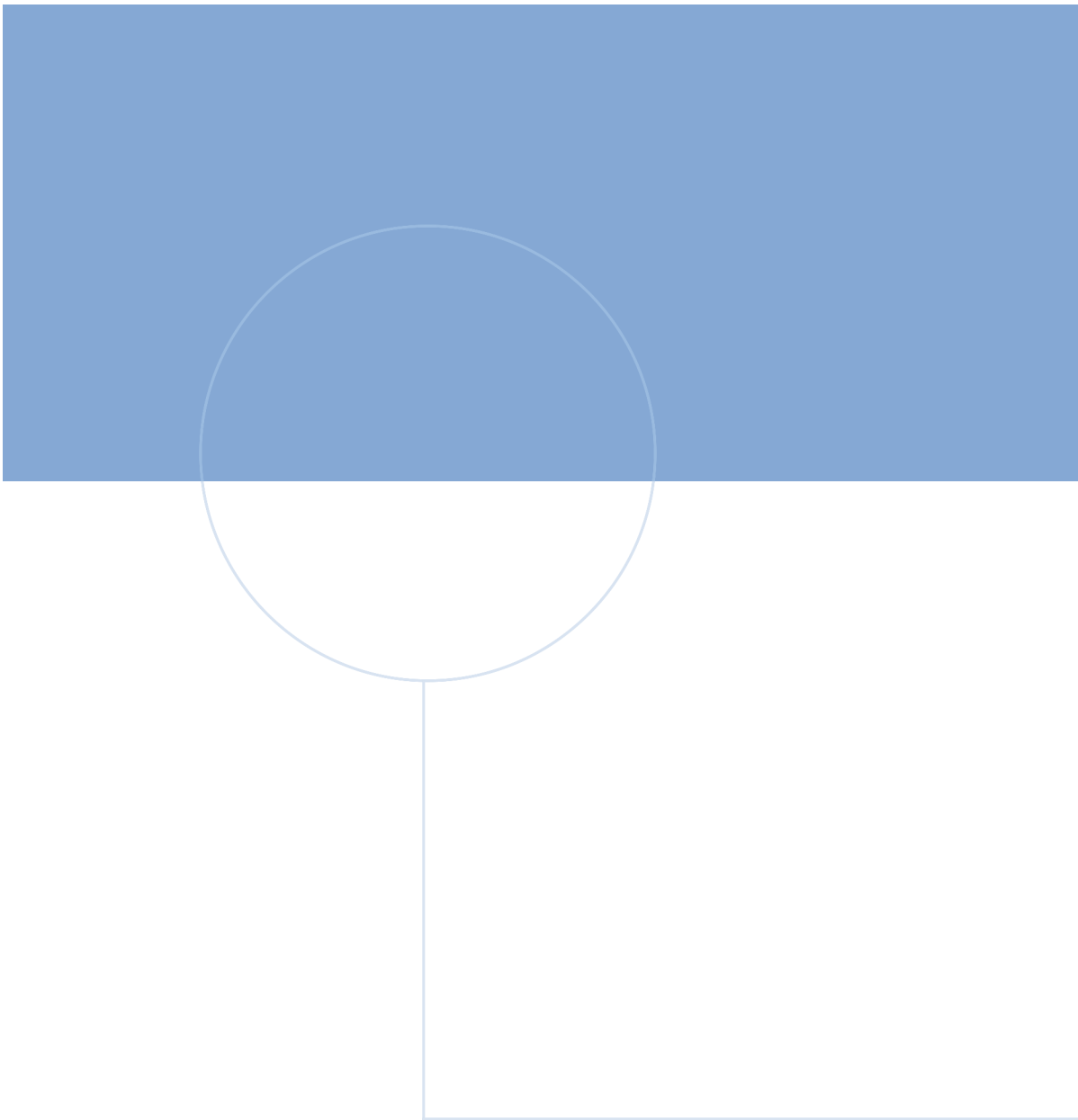

NTNU

Norwegian University of
Science and Technology